Early to Middle Miocene Orbitally-Paced Climate Dynamics in the Eastern Equatorial Atlantic

Bianca R. Spiering[1], Evi Wubben[1], Frederik J. Hilgen[1], and Appy Sluijs[1]

[1]Department of Earth Sciences, Faculty of Geosciences, Utrecht University, Utrecht, The Netherlands.

Corresponding author: Bianca Spiering (b.r.spiering@uu.nl)

Key Points:

- The West African monsoon drove orbitally-paced variations in upwelling intensity, productivity, and dust supply between 18 and 15 Ma.
- Dominant 60-50 kyr cyclicity between 16.9 and 16.3 Ma resulted from precession-obliquity combination tones within a 2.4 Myr eccentricity minimum.
- Asymmetric eccentricity and obliquity cycles suggest an influence of high-latitude, glacial-interglacial variability.

Abstract

Detailed analysis of tropical climate dynamics is lacking for the Early to Middle Miocene, even though this time interval bears important analogies for future climates. Based on high-resolution proxy reconstructions of sea (sub)surface temperature, export productivity and dust supply at Ocean Drilling Program Site 959, we investigate orbital forcing of the West African monsoon in the eastern equatorial Atlantic across the prelude, onset, and continuation of the Miocene Climatic Optimum (MCO; 18-15 Ma). Along with previously identified eccentricity periodicities of ~400 kyr and ~100 kyr, our records show that climate varied on ~27-17 kyr, ~41 kyr, and ~60-50 kyr timescales, which we attribute to precession, obliquity, and their combination tones, respectively. Three intervals with distinct variability were recognized: (1) strong eccentricity, obliquity, and precession variability prior to the MCO (18.2-17.7 Ma), (2) strong influence of obliquity just after the onset of the MCO (16.9-16.3 Ma) concurring with a node in the 2.4 Myr eccentricity cycle, and (3) dominant eccentricity and precession variability during the MCO between 16.3 and 15.0 Ma. Sedimentation at Site 959 was influenced by orbitally-paced variations in upwelling intensity and North African aridity related to West African monsoon dynamics. Continuously present patterns of precession imply low-latitude forcing, while asymmetric eccentricity and obliquity imprints and strong obliquity influence suggest that Site 959 was also affected by high-latitude, glacial-interglacial dynamics.

1 Introduction

The Miocene Climatic Optimum (MCO; ~17-15 Ma) was an interval of global warmth that interrupted the long-term Cenozoic cooling trend recognized in benthic foraminiferal oxygen isotope records (Vincent & Berger, 1985; Westerhold et al., 2020; Woodruff & Savin, 1991). Proxy reconstructions indicate that the MCO was significantly warmer than today (Burls et al., 2021) with atmospheric CO_2 of 400-600 ppm and possibly peak values up to 800-1100 ppm (Foster et al., 2012; Sosdian et al., 2018; Steinthorsdottir et al., 2019; Stoll et al., 2019; Super et al., 2018; Y.G. Zhang et al., 2013). These estimates are comparable to predictions for the near future, making the MCO an interesting analogue for future climate change (Steinthorsdottir et al., 2021). Continuous, high-resolution records for the Early to Middle Miocene are, however, limited to benthic foraminiferal stable carbon and oxygen isotope records describing deep-ocean and high-latitude environments (Steinthorsdottir et al., 2021), while high-resolution records on tropical (monsoon) dynamics are lacking.

The West African monsoon is one of Earth's regional monsoon systems that dominates hydrological cycling and zonal heat gradients in the Atlantic Ocean. Sediments from the Mediterranean Sea, the subtropical Atlantic off Northwest Africa, and the eastern equatorial Atlantic (Figure 1a) revealed that the West African monsoon responded strongly to orbital forcing. Pleistocene to Late Miocene sapropel-marl deposits in the Mediterranean are widely acknowledged to reflect orbitally-forced variations between humid and dry North African climate states (e.g., Lourens et al., 2001; Rossignol-Strick, 1983; Schenau et al., 1999). Inferred wet-dry variations also show an established West African monsoon off Northwest Africa for the past 5 Myr (Tiedemann et al., 1994) and in the eastern equatorial Atlantic between 2 and 6 Ma (Vallé et al., 2017).

Climate simulations (for <1 Ma) imply that the sedimentary observations are indeed consistent with the response of the African monsoon to orbital forcing through variability in atmospheric and hydrologic circulation (Bosmans, Drijfhout, et al., 2015; Bosmans, Hilgen, et

al., 2015). Both sediments and models indicate that precession, which dominates insolation changes at low latitudes, was the main driver of monsoon variability (Bosmans, Drijfhout, et al., 2015). However, pronounced obliquity and eccentricity signals in Pleistocene monsoon proxies indicate that the tropical climate was also affected by northern hemisphere glaciations (Bloemendal & deMenocal, 1989; deMenocal et al., 1993; Tiedemann et al., 1994), which has been confirmed by modelling studies (Weber & Teunter, 2011).

Further back in time, during the Eocene, Paleocene, and Cretaceous in the eastern equatorial Atlantic, precession cycles in organic carbon content (Cramwinckel et al., 2018; Frieling et al., 2019), ascribed to wet-dry oscillations for the Cretaceous (Beckmann et al., 2005), suggest the presence of a monsoon, although it presumably operated differently from the modern system due to the land-sea distribution (Beckmann et al., 2005). Interestingly, simulations suggest that the Atlantic Ocean was too narrow during the Cretaceous and early Cenozoic for a pronounced West African monsoon, suggesting it only developed during the mid-Cenozoic as the Atlantic basin expanded (Acosta et al., 2022). These simulations also suggest the presence of a West African monsoon during the Middle Miocene and an intensification with increasing atmospheric CO_2 concentrations, but observations to test this inference are lacking. It remains unknown what the nature and importance was of the West African monsoon during the Early and Middle Miocene, how it responded to the onset of the MCO, and if it was affected by ice sheet dynamics like in the Pleistocene.

To address this knowledge gap, we investigate potentially monsoon-related orbital cyclicity in the Early to Middle Miocene using sediments recovered at Ocean Drilling Program (ODP) Site 959 in the eastern equatorial Atlantic (Figure 1; Mascle et al., 1996). This site has previously been used to study monsoon variability in other time periods on non-orbital (Norris, 1998a; Wagner, 1998, 2002) and orbital timescales (Beckmann et al., 2005; Vallé et al., 2017). A recent age model for the Lower to Middle Miocene sediments collected at Site 959 showed that a near-complete 18-15 Ma section was recovered, suitable for assessing climate variability at precession to eccentricity timescales (Wubben et al., 2023). We use records of sediment color, magnetic susceptibility (MS), bulk carbonate stable carbon and oxygen isotopic composition ($\delta^{13}C$ and $\delta^{18}O$) and weight percent (wt%) $CaCO_3$ published in Wubben et al. (2023), biomarker paleothermometer data from a companion paper (Wubben et al., submitted), as well as newly presented bulk sediment elemental composition data (biogenic Ba, Ti/Al, and V/Al). Detailed frequency analysis is performed on these high-resolution records to investigate the response to orbital forcing across the prelude, onset, and continuation of the MCO. Subsequently, the nature of potential monsoon-forcing is evaluated on different orbital timescales.

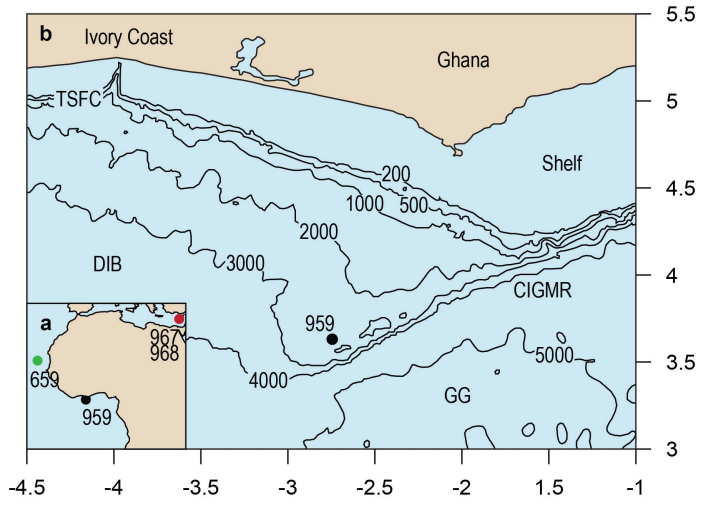

Figure 1. Location maps of Site 959: (**a**) map showing the position of Site 959 in the eastern equatorial Atlantic, Site 659 in the subtropical Atlantic off Northwest Africa, and Sites 967-968 in the eastern Mediterranean, and (**b**) bathymetric map of Site 959 with depth contour lines in meters. Bathymetry is based on data from GEBCO Bathymetric Compilation Group (2022). Abbreviations: CIGMR = Côte d'Ivoire-Ghana Marginal Ridge, DIB = Deep Ivorian Basin, GG = Gulf of Guinea, TSFC = Trou Sans Fond Canyon.

2 Setting of ODP Site 959

ODP Hole 959A is located in the eastern equatorial Atlantic Ocean ~120 km offshore Ivory Coast (latitude 3.627650, longitude -2.735200; Figure 1; Mascle et al., 1996). The site was drilled at 2102 m water depth on the southern edge of the Deep Ivorian Basin (DIB), just north of the top of the Côte d'Ivoire-Ghana Marginal Ridge (CIGMR). The CIGMR and DIB were formed due to the opening of the equatorial Atlantic during the Early Cretaceous (Basile et al., 1993). The relatively shallow bathymetric position on the slope of the marginal ridge allowed the recovery of relatively unaltered and undisturbed sediments.

Site 959 is suitable for studying monsoon dynamics as it is located in a region sensitive to seasonal shifts of the latitudinal position of the Intertropical Convergence Zone (ITCZ; Figure 2). During boreal summer (Figure 2a), the ITCZ is centered over the North African continent at ~18°N and southwest (SW) monsoons carry moisture from the tropical Atlantic into North Africa (Trauth et al., 2009). During boreal winter (Figure 2b), the ITCZ shifts southward to the Guinea coast and into the southern hemisphere African continent. In this period, surface airflow over North Africa is dominated by the northeast (NE) trade winds. A specific component of the NE trades, the Harmattan, transports dust from the Bodélé depression in Chad to the equatorial Atlantic (Prospero et al., 2002; Stuut et al., 2005; Trauth et al., 2009).

The Comoé River discharges into the Gulf of Guinea on the east side of Ivory Coast. However, sediment transport is effectively canalized by the Trou Sans Fond Canyon (TSFC), probably since the Oligocene, and therefore does not significantly influence Site 959 (Figure 1; Droz et al., 1985; Wagner, 1998). The main currents in the equatorial Atlantic are the westward flowing South Equatorial Current (SEC) and the eastward flowing Equatorial Undercurrent (EUC; Figures 2a & b; Norris, 1998a). The EUC carries cool, saline water from the South

Atlantic and is deflected northwards into the Gulf of Guinea, producing a strong thermocline (Norris, 1998a). The Guinea current flows eastward into the Gulf of Guinea and is enforced by the North Equatorial Countercurrent (NECC) during boreal summer when the ITCZ moves northward (Figure 2a; Norris, 1998a). Prior to the establishment of the Guinea Current at ~5 Ma, it was hindered by a too southerly position of the Guinea coast (<2.5°N; Norris, 1998a), which was most likely also the case for the Early and Middle Miocene. In the eastern equatorial Atlantic, oceanic upwelling occurs along the Equatorial Divergence Zone (Wagner, 1998) and wind-induced coastal upwelling occurs off Ivory Coast and Ghana during boreal summer due to the combination of the Guinea Current and winds flowing parallel along the coast (Figure 2a; Norris, 1998a; Vallé et al., 2017; Wagner, 1998). A minor coastal upwelling event occurs during boreal winter due to the displacement of the ITCZ and corresponding wind systems (Wagner, 1998, 2002). Present-day sea surface temperatures (SSTs) in the Gulf of Guinea vary seasonally between ~25°C during the summer upwelling season, and ~29°C in winter (Djakouré et al., 2017).

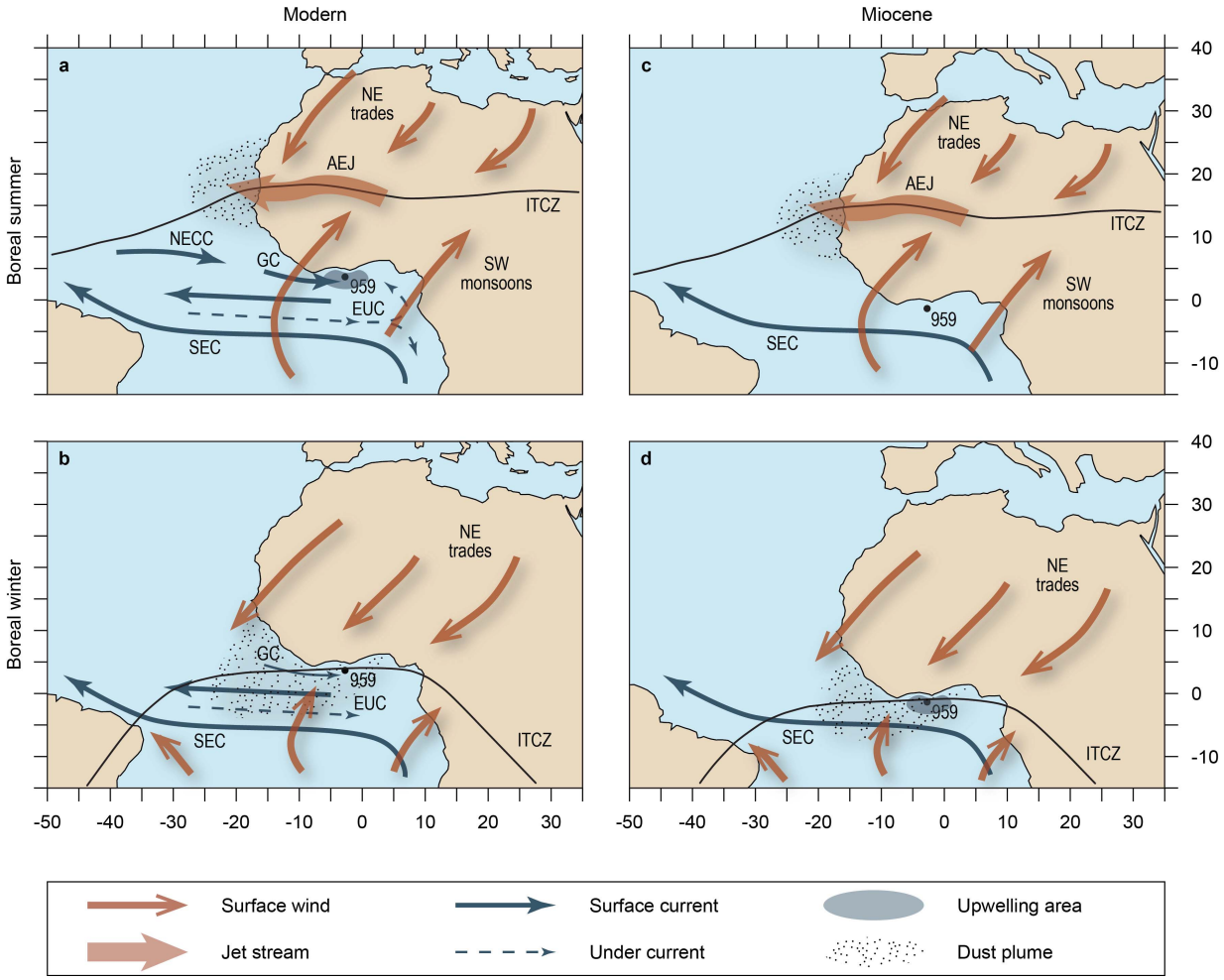

Figure 2. Maps with generalized atmospheric and oceanic circulation patterns around North Africa: modern situation for (**a**) boreal summer and (**b**) boreal winter (after Wang, 2009; Wagner, 1998; Norris, 1998a), and hypothesized Early to Middle Miocene situation for (**c**) boreal summer and (**d**) boreal winter. The continental boundaries are based on a 17 Ma

reconstruction using GPlates (Müller et al., 2018) with plate reconstructions of Seton et al. (2012) and paleomagnetic reference frame of Torsvik et al. (2012). At 17 Ma, Site 959 was located at a latitude of ~1°S +/- 2.5°. Abbreviations: NE = northeast, SW = southwest, AEJ = African Easterly Jet, ITCZ = Intertropical Convergence Zone, NECC = North Equatorial Countercurrent, GC = Guinea Current, SEC = South Equatorial Current, EUC = Equatorial Undercurrent.

3 Materials and Methods

3.1 Sediment properties

Lower to Middle Miocene sediments from ODP Hole 959A, cores 21X to 27X span 189 to 255 meters below sea floor (mbsf) and represent nannofossil chalks and clays with some organic matter, which are interbedded with diatomites in the lower part (cores 23X to 27X; 208 to 255 mbsf; Mascle et al., 1996; Wagner, 2002). Alternations in sediment color were observed from light to dark on 10 to 80 cm scale, in which siliceous phases generally represent the darker lithology and clay/calcareous phases represent the lighter lithology (Mascle et al., 1996).

3.2 Age model

Recently, a revised mbsf (rmbsf) depth scale was established by assuming 0.5 m gaps at core breaks (Wubben et al., 2023). Additionally, shipboard age control (Mascle et al., 1996; Norris, 1998b; Shafik et al., 1998) was updated with diatom and calcareous nannofossil biostratigraphy and chemostratigraphic markers (Figure 3; Wubben et al., 2023). These include the ~0.5‰ $\delta^{18}O$ decrease at the onset of the MCO (16.9 Ma), the Monterey positive $\delta^{13}C$ excursion, carbon-isotope maxima (CM) 1-4, and the MCO 'peak warming' event at 15.6 Ma (Figure 3; Wubben et al., 2023), which all have orbitally-tuned ages (Holbourn et al., 2007; Holbourn et al., 2015). Spectral analysis in the depth domain revealed main periodicities of ~12.5-10 m, ~3.5-2.5 m, ~1.5-1 m, and ~0.65-0.45 m, which were linked to ~400 kyr eccentricity, ~100 kyr eccentricity, obliquity (~41 kyr), and precession (~23-19 kyr), respectively (Wubben et al., 2023).

The bulk carbonate $\delta^{13}C$ record was chosen for orbital tuning because of the clear expression of ~400 and ~100 kyr eccentricity (Wubben et al., 2023). Pronounced $\delta^{13}C$ minima were correlated to ~100 kyr eccentricity maxima (Figure 3), consistent with previous work (Holbourn et al., 2007; Liebrand et al., 2016; Pälike et al., 2006). Tuning of the interval after the onset of the MCO (17-15 Ma) was relatively straightforward and the resulting age model corresponds well with the bio- and chemostratigraphy (Figure 3). It was inferred that a ~100 kyr eccentricity maximum is missing between cores 22X and 23X (~227 rmbsf), resulting in a gap of ~60 kyr (Wubben et al., 2023). No significant amount of time is missing in the other core gaps.

Tuning of the pre-MCO interval (>17 Ma) was more complicated due to a discrepancy between diatom and calcareous nannofossil biostratigraphic tie-points (Wubben et al., 2023). Ultimately, the calcareous nannofossil tie-points were used because of their good constraints in the western equatorial Atlantic biostratigraphy, resulting in a hiatus of ~750 kyr between cores 25X and 26X (~258 rmbsf; Wubben et al., 2023). Despite the uncertainty in absolute age control, the clear recognition of ~100 kyr eccentricity-related $\delta^{13}C$ variations provides a confident relative age control for further cyclostratigraphic analyses. The age model indicates that the studied interval (cores 21X-27X) covers 15.0-16.9 Ma and 17.7-18.2 Ma with average

sedimentation rates of ~2.6 cm/kyr and ~3.7 cm/kyr, respectively. Spectral analysis in the time domain was mainly focused on periodicities of >100 kyr, while higher frequencies were not yet investigated in detail (Wubben et al., 2023).

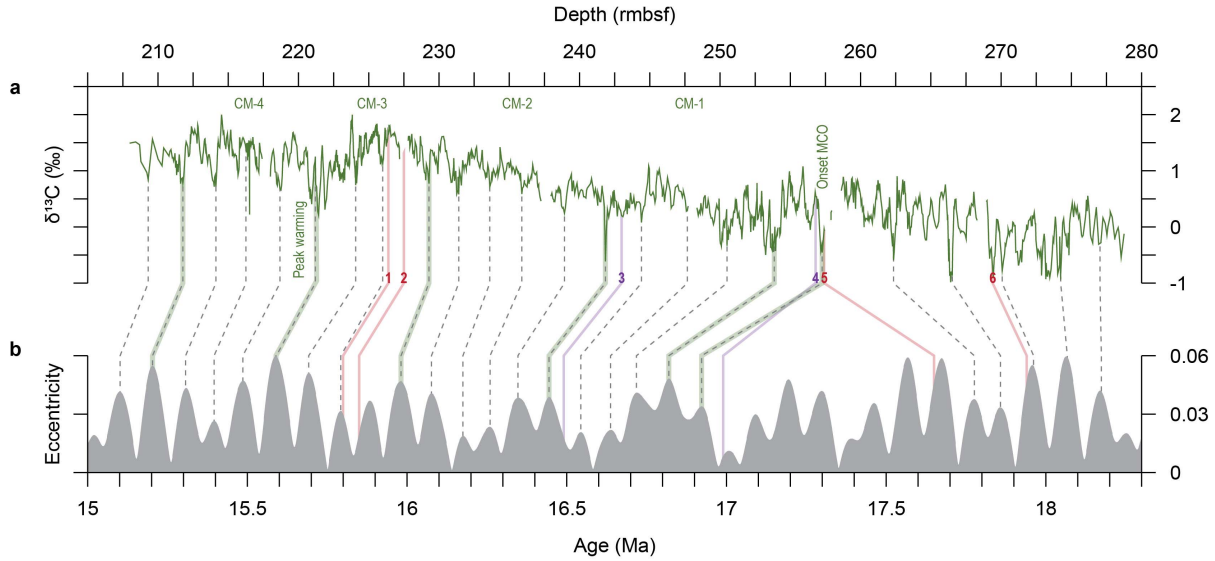

Figure 3. Orbital tuning of the bulk carbonate $\delta^{13}C$ record. Tie-points (dashed gray lines; Wubben et al., 2023) connect pronounced minima in the $\delta^{13}C$ record in the depth domain (**a**) to eccentricity maxima in the La2004 eccentricity solution (**b**; Laskar et al., 2004). Positions and ages of nannofossil, diatom, and chemostratigraphic markers are indicated by the red, purple, and green lines, respectively (Wubben et al., 2023). Numbered biostratigraphic markers: 1 = top common D. *deflandrei*, 2 = bottom D. *signus*, 3 = top R. *marylandicus*, 4 = bottom A. *californicus* and C. *coscinodiscus*, 5 = bottom common S. *heteromorphus* (minimum depth), 6 = top S. *belemnos*.

3.3 Previously published proxy records

The sediment color, magnetic susceptibility (MS), bulk carbonate stable carbon and oxygen isotopic ratios ($\delta^{13}C$ and $\delta^{18}O$) and wt% $CaCO_3$ records of Wubben et al. (2023) have an average resolution of 1 cm (<1 kyr), 3 cm (1 kyr), 5 cm (2 kyr) and 15 cm (5 kyr), respectively (Figure 4). A record of the tetraether index of tetraethers with 86 carbon atoms (TEX_{86}; Schouten et al., 2002), which is positively correlated to sea (sub)surface temperature, was generated by Wubben et al. (submitted) at an average resolution of 13 cm (4 kyr). We also consider their record of the branched and isoprenoid tetraether (BIT) index (Hopmans et al., 2004) for soil-derived biomarker inputs. TEX_{86} values with a BIT index above 0.4 (n = 7) were removed as they are considered unreliable (Weijers et al., 2006). See Wubben et al. (submitted) for a detailed description of the biomarker data.

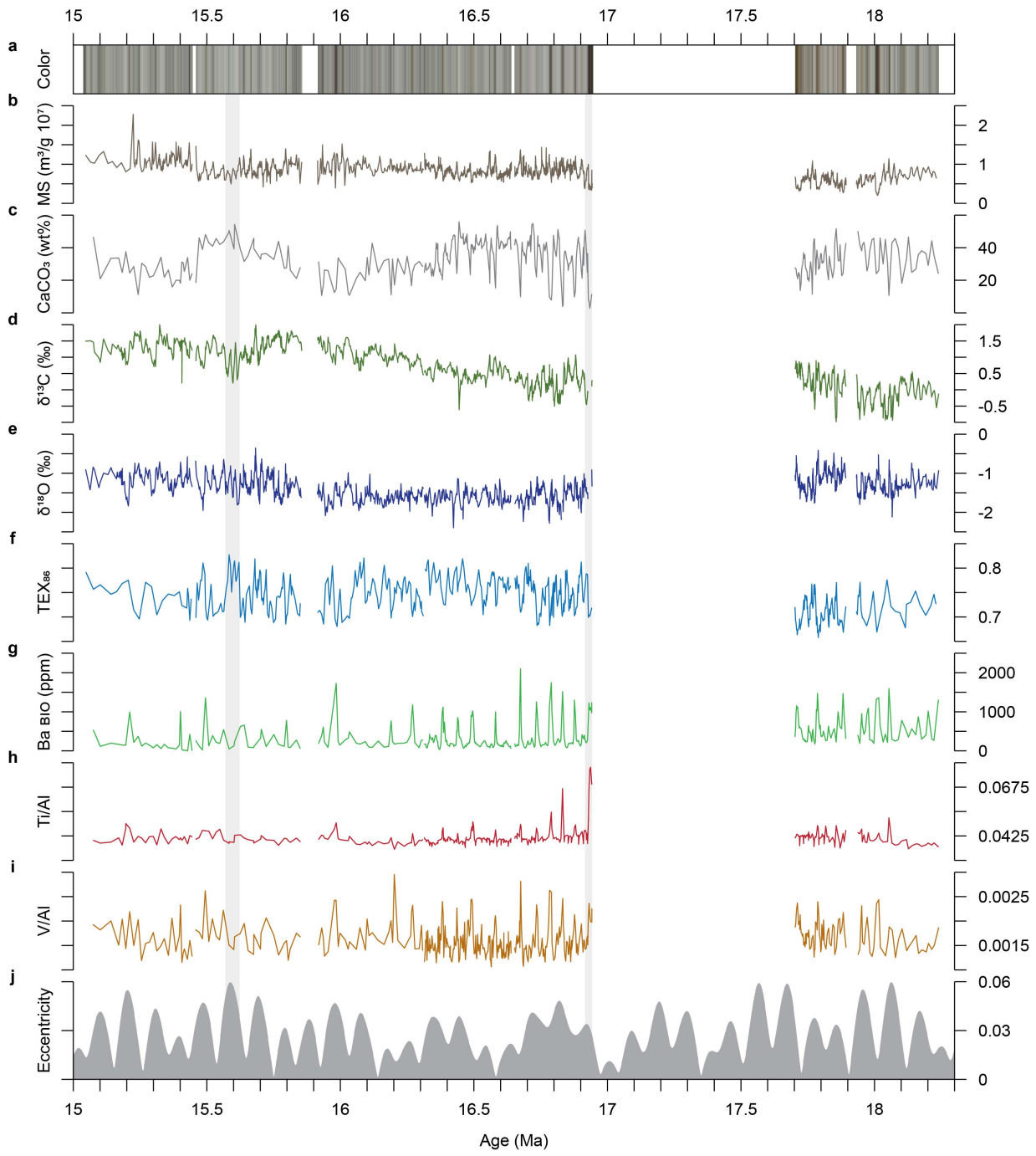
15
15.5
16
16.5
17
17.5
18
a
Color
b
MS (m³/g 10⁷)
2
1
0
c
CaCO₃ (wt%)
40
20
d
δ¹³C (‰)
1.5
0.5
-0.5
e
δ¹⁸O (‰)
0
-1
-2
f
TEX₈₆
0.8
0.7
g
Ba BIO (ppm)
2000
1000
0
h
Ti/Al
0.0675
0.0425
i
V/Al
0.0025
0.0015
j
Eccentricity
0.06
0.03
0
Age (Ma)

207

Figure 4. Overview of Early to Middle Miocene proxy data from Site 959: (**a**) color, (**b**) MS, (**c**) wt% $CaCO_3$, (**d**) $\delta^{13}C$, (**e**) $\delta^{18}O$, (**f**) TEX_{86}, (**g**) Ba_{bio}, (**h**) Ti/Al, (**i**) V/Al, and (**j**) the La2004 eccentricity solution (Laskar et al., 2004). The gray bars represent the onset of the MCO at 16.9 Ma and the MCO 'peak warming' event at 15.6 Ma.

3.4 Bulk sediment elemental concentrations

Quantitative bulk elemental composition was measured with Inductively Coupled Plasma – Optical Emission Spectroscopy (ICP-OES) by Wubben et al. (2023) at an average resolution of 15 cm (5 kyr). The measured concentrations of Al, Ba, Ti and V (in ppm) were used to generate new geochemical records. Al was used as normalization parameter as it generally behaves conservatively (Calvert & Pedersen, 2007). The average recovery (accuracy) of Al, Ba, Ti and V was 99-106%, 91-102%, 100-106% and 83-101%, respectively. For all elements, the average analytical uncertainty based on duplicates was ~1%.

We used the concentration of biogenic Ba (Ba_{bio}) as a proxy for (export) productivity (Dymond et al., 1992; Kasten et al., 2001; Piela et al., 2012). At sites with significant terrestrial input, the barium signal in sediments may be strongly influenced by detrital barium present in aluminosilicates (Dymond et al., 1992). The Ba_{bio} signal was estimated by correcting the measured total Ba concentration for the detrital contribution (Dymond et al., 1992):

$$Ba_{bio} = Ba_{total} - \left(Al \times \left(\frac{Ba}{Al}\right)_{detrital}\right)$$

We determined a $(Ba/Al)_{detrital}$ value of 0.0029, as this resulted the lowest positive Ba_{bio} values (i.e., a value >0.0029 resulted in negative Ba_{bio} values). Although this value is lower than the 0.005-0.01 range based on the average crustal composition, it falls within the range of values obtained directly by sequential extraction for various sites in the Atlantic (0.0014-0.0041; Reitz et al., 2004).

The Ti/Al ratio was used as a proxy for aeolian (versus fluvial) input and sediment grain-size (Calvert & Pedersen, 2007; Govin et al., 2012; Martinez-Ruiz et al., 2015). Ti in aeolian dust mainly resides in heavy minerals, which are transported along with coarser quartz grains (Calvert & Pedersen, 2007; Martinez-Ruiz et al., 2015). The V/Al ratio was as a proxy for redox state. V is sensitive to minor changes in oxygen concentration and starts to accumulate as oxyhydroxides under dysoxic to suboxic conditions, in the absence of oxygen and sulfide (Calvert & Pedersen, 2007; Martinez-Ruiz et al., 2015).

3.5 Spectral analysis

The data was analyzed in the time domain using the orbitally-tuned age model presented by Wubben et al. (2023). Time series were sorted, interpolated to uniform spacing, and detrended to remove long-term trends using Acycle (Li et al., 2019). Depending on the time series, detrending was done linearly or using the locally weighted regression smoothing (LOWESS) method. Power spectra were generated with the multitaper method (time-bandwidth product = 2, pad factor = 5; Thomson, 1982) and first-order autoregressive (AR1) noise confidence levels (Meyers, 2012) using Astrochron (Meyers, 2014). Bandpass filtering was applied to isolate specific frequency components present in the time series using the Gauss algorithm in Acycle (Li et al., 2019).

For some intervals of the elemental (15.0-16.3 Ma and 17.9-18.2 Ma) and TEX_{86} data (15.0-15.4 Ma and 17.9-18.2 Ma), high-frequency analyses were not possible due to the relatively low resolution (~10-20 kyr). The color record, although providing valuable information on light-dark variations, is not used for spectral analyses as uneven lighting during shipboard core photography likely introduced artificial variability related to section and core length (Wubben et al., 2023).

4 Results

4.1 Elemental concentrations

Al concentrations are on average 6×10^4 ppm, varying between 2×10^4 ppm and 10×10^4 ppm (Figure S1). The Al record is very similar to the MS record in terms of trends and variability, with high Al corresponding to high MS (Figure S2e).

Ba concentrations vary between 2×10^2 ppm and 23×10^2 ppm (Figure S1) and Ba_{bio} concentrations vary between 0 ppm and 21×10^2 ppm (Figure 4). Besides the difference in concentration, the Ba and Ba_{bio} records seem identical, implying that most of the Ba variability is related to Ba_{bio}. The Ba_{bio} record is characterized by pronounced peaks of $>8 \times 10^2$ ppm that occur regularly and generally correspond to darker sediment layers. Peaks are less well defined between 18.2-17.9 Ma and 16.3-15.0 Ma, possibly due to the lower sampling resolution.

Ti concentrations vary between 1×10^3 ppm and 4×10^3 ppm (Figure S1) and Ti/Al ratios vary between 4×10^{-2} and 8×10^{-2} (Figure 4). The Ti record displays similar trends and variability as the Al record. Al-normalization results in a pattern with pronounced, regularly-occurring peaks between 16.9-16.3 Ma, similar to the Ba_{bio} record. The two largest Ti/Al peaks occur just after the onset of the MCO (16.9-16.8 Ma) with values of $>6 \times 10^{-2}$. The pre-MCO between 17.9-17.7 Ma displays smaller-scale variability and is characterized by a series of sharp minima.

V concentrations vary between 5×10^1 ppm and 21×10^1 ppm (Figure S1) and V/Al ratios vary between 1×10^{-3} and 3×10^{-3} (Figure 4). The V record is relatively similar to the Al record, although V displays some relatively more pronounced peaks in the interval 16.9-16.3 Ma, which become slightly more pronounced after Al-normalization.

4.2 Orbital variability in the proxy records

The Early to Middle Miocene proxy records of Site 959 show variability on scales of ~400 kyr, ~100 kyr, ~60-40 kyr, and ~27-17 kyr (Figure 4). Significant spectral power is found in these four frequency bands (Figure S3), consistent with the results of Wubben et al. (2023). Maxima of $\delta^{13}C$ generally correspond to maxima of $\delta^{18}O$, Ba_{bio}, Ti/Al, and V/Al, minima of wt% $CaCO_3$ and TEX_{86}, and darker sediment layers which are likely rich in biogenic silica (Figure 4). However, variability differs between proxy records and changes through time (Figure 5). Significant ~60-40 kyr variability following the onset of the MCO (16.9-16.3 Ma) deviates from the strong ~100 kyr pacing during the pre-MCO (18.2-17.7 Ma) and later part of the MCO (16.3-15.0 Ma). Because of these significant differences in variability, the records are divided in three intervals: (1) 18.2-17.7 Ma, (2) 16.9-16.3 Ma, and (3) 16.3-15.0 Ma.

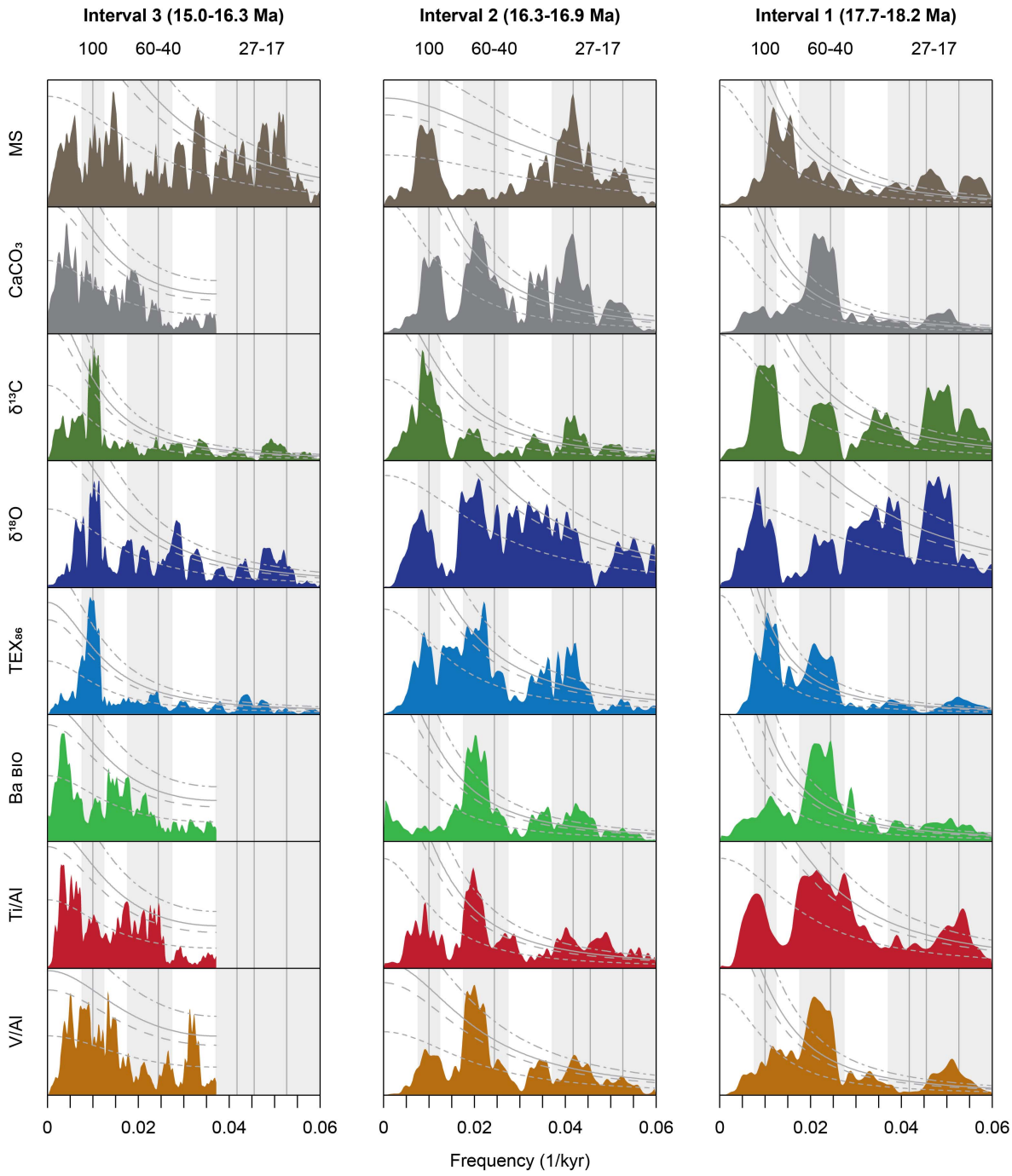
Interval 3 (15.0-16.3 Ma)
Interval 2 (16.3-16.9 Ma)
Interval 1 (17.7-18.2 Ma)
100
60-40
27-17
MS
CaCO3
δ13C
δ18O
TEX86
Ba BIO
Ti/Al
V/Al
0
0.02
0.04
0.06
Frequency (1/kyr)

286

Figure 5. Power spectra of Site 959 proxy data for three intervals: 18.2-17.7 Ma, 16.9-16.3 Ma, and 16.3-15.0 Ma. A linear scale in used for both axes. AR1 fit, and 90%, 95%, and 99% confidence levels are indicated by the small dashed, large dashed, solid, small-large dashed gray lines, respectively. The gray bars indicate important frequency bands representing periodicities of ~100 kyr, ~60-40 kyr, and ~27-17 kyr. The vertical gray lines indicate exact frequencies of 1/100, 1/41, 1/24, 1/22, 1/19 1/kyr.

4.2.1 Interval 1 (18.2-17.7 Ma)

Before the onset of the MCO, the proxy records display strong variability on scales of ~100 kyr, ~60-40 kyr, and ~27-17 kyr (Figures 5 & 6). Records of $\delta^{13}C$, $\delta^{18}O$, TEX_{86} and MS display clear ~100 kyr cyclicity, but spectral power only reaches above the 95% confidence level for TEX_{86}. In the TEX_{86} record, ~100 kyr variability is asymmetrical between 17.9 and 17.7 Ma. This is characterized by a steep increase during high eccentricity followed by a gradual decrease with lower eccentricity, punctuated by smaller-scale fluctuations. The two rapid increases of TEX_{86} at ~17.86 and ~17.78 Ma concur with the two rapid and pronounced decreases of $\delta^{13}C$. Although ~100 kyr cyclicity is insignificant in records of wt% $CaCO_3$, Ba_{bio}, Ti/Al and V/Al, clear ~100 kyr variability can be recognized in the Ba_{bio} and V/Al records between 17.9 and 17.7 Ma.

~60-40 kyr cyclicity dominates records of wt% $CaCO_3$, Ba_{bio}, Ti/Al and V/Al, but it is also significantly present in $\delta^{13}C$ and TEX_{86}. A change in dominant pacing is observed in the Ba_{bio} and sediment color records, from ~60-40 kyr between 18.2 and 17.9 Ma to ~100 kyr between 17.9 and 17.7 Ma.

Significant spectral power in the ~27-17 kyr band is present in all proxy records. However, between 18.2 and 17.9 Ma, the resolution of the elemental and TEX_{86} records is insufficient to record variations on this scale. Bandpass filtering reveals that greater amplitudes of the ~27-17 kyr cycle roughly correspond to eccentricity maxima, most clearly visible in records of $\delta^{13}C$ and $\delta^{18}O$ (Figure 6).

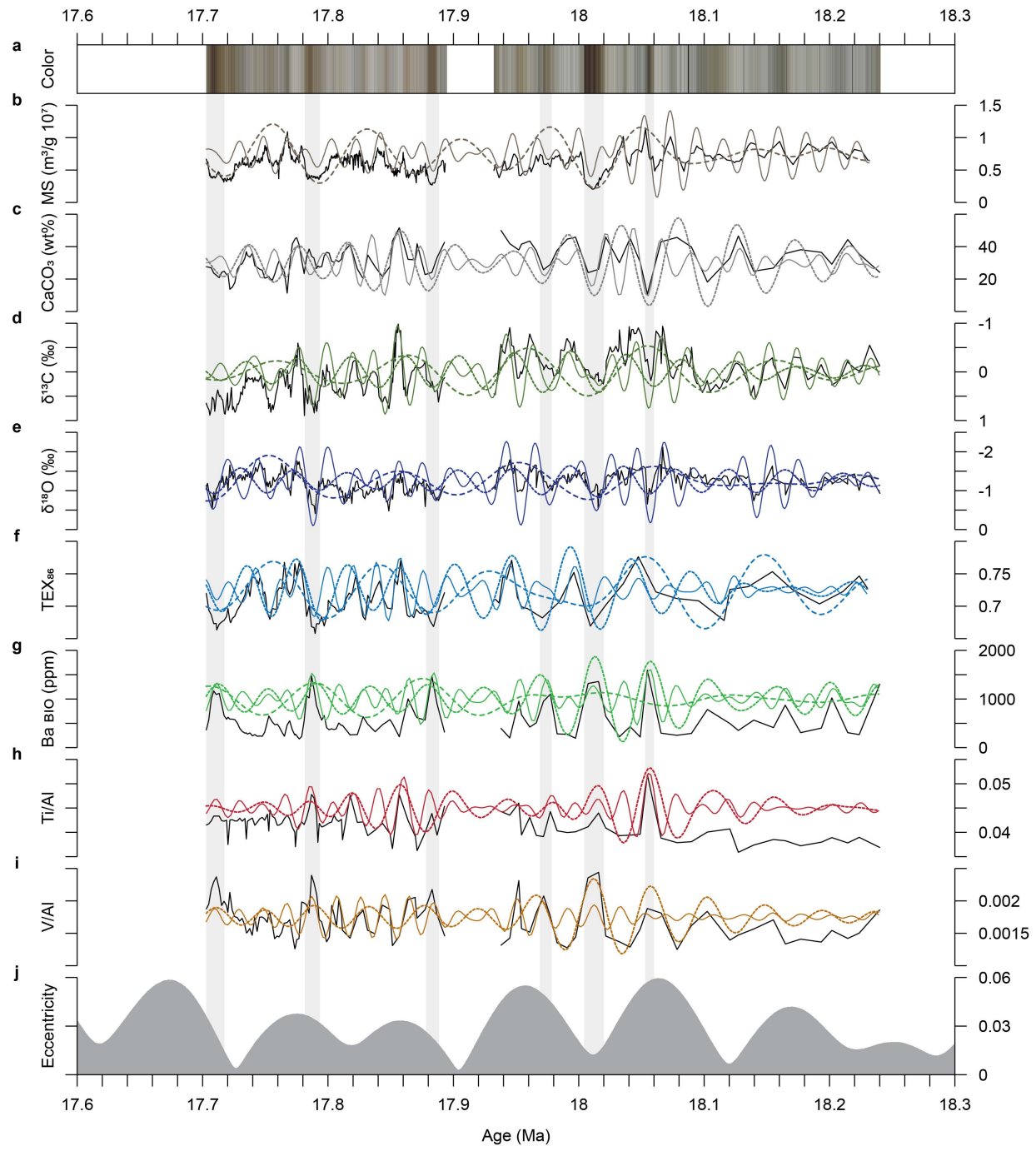

Figure 6. Interval 1 (18.2-17.7 Ma) with Site 959 proxy data and bandpass filters: (**a**) color, (**b**) MS, (**c**) $CaCO_3$, (**d**) $\delta^{13}C$, (**e**) $\delta^{18}O$, (**f**) TEX_{86}, (**g**) Ba_{bio}, (**h**) Ti/Al, (**i**) V/Al, and (**j**) the La2004 eccentricity solution (Laskar et al., 2004). The gray bars indicate relatively dark sediment layers that correspond to peaks of Ba_{bio}. Bandpass filters of ~100 kyr, ~60-40 kyr, and ~27-17 kyr cyclicity are represented by dashed, dotted, and solid colored lines, respectively. The following bandpass filter widths (in 1/kyr) were used: 0.0086-0.017 and 0.036-0.061 for MS, 0.006-0.014, 0.018-0.027 and 0.03-0.061 for $\delta^{13}C$, 0.0055-0.014, 0.019-0.0265 and 0.03-0.058 for $\delta^{18}O$, 0.017-0.028 and 0.036-0.06 for $CaCO_3$, 0.007-0.014, 0.0175-0.028 and 0.035-0.06 for TEX_{86},

0.007-0.014, 0.017-0.0275 and 0.036-0.06 for Ba_{bio}, 0.016-0.03, 0.036-0.06 for Ti/Al, and 0.017-0.027 and 0.04-0.06 for V/Al.

4.2.2 Interval 2 (16.9-16.3 Ma)

The $\delta^{13}C$ record displays clear ~100 kyr cyclicity (Figure 7), which almost reaches above the 95% confidence level (Figure 5). Relatively weak power around this period is found in records of $\delta^{18}O$, wt% $CaCO_3$, MS, TEX_{86}, Ti/Al, and V/Al. For TEX_{86}, two clear ~100 kyr cycles can be recognized between ~16.5 and ~16.3 Ma (in the upper part of this interval). The Ba_{bio} record displays no peak in spectral power around a period of ~100 kyr.

The records of wt% $CaCO_3$, TEX_{86}, Ba_{bio}, Ti/Al, V/Al, and sediment color are characterized by significant ~60-50 kyr variability, which is absent in records of $\delta^{13}C$, $\delta^{18}O$, and MS (Figures 5 & 7). Bandpass filters centered at ~60-50 kyr follow the pronounced peaks of Ba_{bio}, Ti/Al, and V/Al, minima of wt%$CaCO_3$ and TEX_{86}, and darker sediment layers. The ~60-50 kyr TEX_{86} cycle around ~16.76 Ma has an asymmetric shape. All proxy records display significant spectral power in the ~27-17 kyr periodicity band. Bandpass filtering reveals that two or three ~27-17 kyr cycles are present within one ~60-50 kyr cycle.

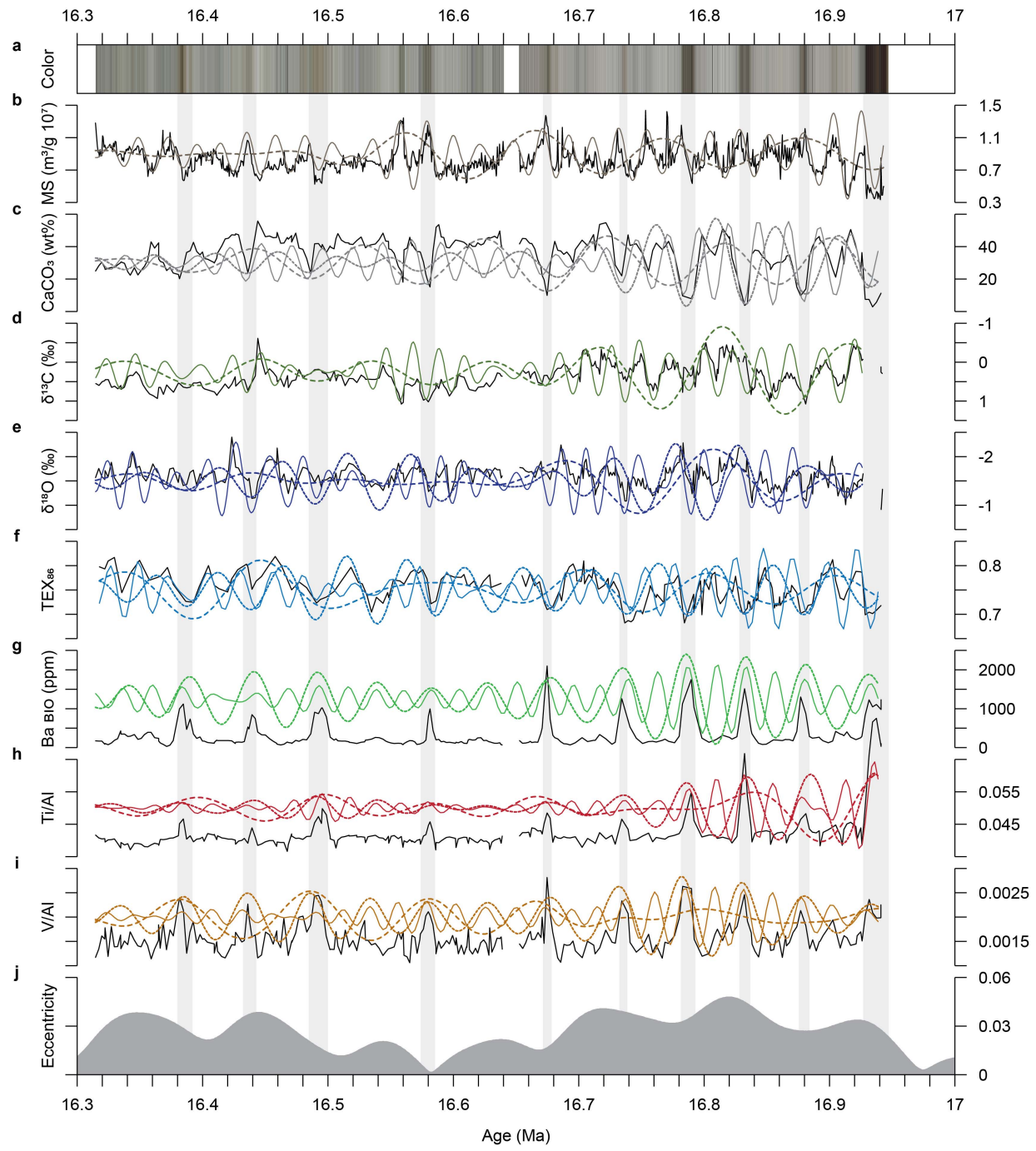

Figure 7. Interval 2 (16.9-16.3 Ma) with Site 959 proxy data and bandpass filters: (**a**) color, (**b**) MS, (**c**) $CaCO_3$, (**d**) $\delta^{13}C$, (**e**) $\delta^{18}O$, (**f**) TEX_{86}, (**g**) Ba_{bio}, (**h**) Ti/Al, (**i**) V/Al, and (**j**) the La2004 eccentricity solution (Laskar et al., 2004). The gray bars indicate relatively dark sediment layers that correspond to peaks of Ba_{bio}. Bandpass filters of ~100 kyr, ~60-40 kyr, and ~27-17 kyr cyclicity are represented by dashed, dotted, and solid colored lines, respectively. The following bandpass filter widths (in 1/kyr) were used: 0.006-0.013 and 0.037-0.055 for MS, 0.007-0.0135 and 0.037-0.055 for $\delta^{13}C$, 0.005-0.012, 0.0155-0.0235 and 0.037-0.0577 for $\delta^{18}O$, 0.007-0.014, 0.0165-0.024 and 0.037-0.047 for $CaCO_3$, 0.006-0.012, 0.017-0.024 and 0.037-0.055 for TEX_{86},

0.0165-0.024 and 0.038-0.048 for Ba_{bio}, 0.006-0.014, 0.0165-0.024 and 0.037-0.0515 for Ti/Al, and 0.006-0.014, 0.0165-0.024 and 0.038-0.048 for V/Al.

4.2.3 Interval 3 (16.3-15.0 Ma)

After 16.3 Ma, the high-resolution proxy records are dominated by ~100 kyr and ~27-17 kyr variability (Figures 5 & 8). Significant ~100 kyr cyclicity is present in records of $\delta^{13}C$, $\delta^{18}O$, and TEX_{86}. The amplitude of the ~100 kyr cycle in TEX_{86} follows the orbital solution of eccentricity, with greater amplitudes corresponding to ~400 kyr eccentricity maxima. Additionally, the TEX_{86} record shows significant ~41 kyr cyclicity, which follows relatively pronounced TEX_{86} minima, and greater amplitudes occur during ~400 kyr eccentricity minima. Although power at ~100 kyr is not significant for Ti/Al, this cycle does approximately follow orbital eccentricity.

All high-resolution records (i.e., $\delta^{13}C$, $\delta^{18}O$, TEX_{86}, and MS) display significant ~27-17 kyr cyclicity. For $\delta^{13}C$ and $\delta^{18}O$, greater amplitudes of the ~27-17 kyr cycle generally correspond with ~100 kyr eccentricity maxima, particularly during the 15.6 Ma 'peak warming' event. This event corresponds to an interval with a relatively light sediment color and shows relatively high TEX_{86} values.

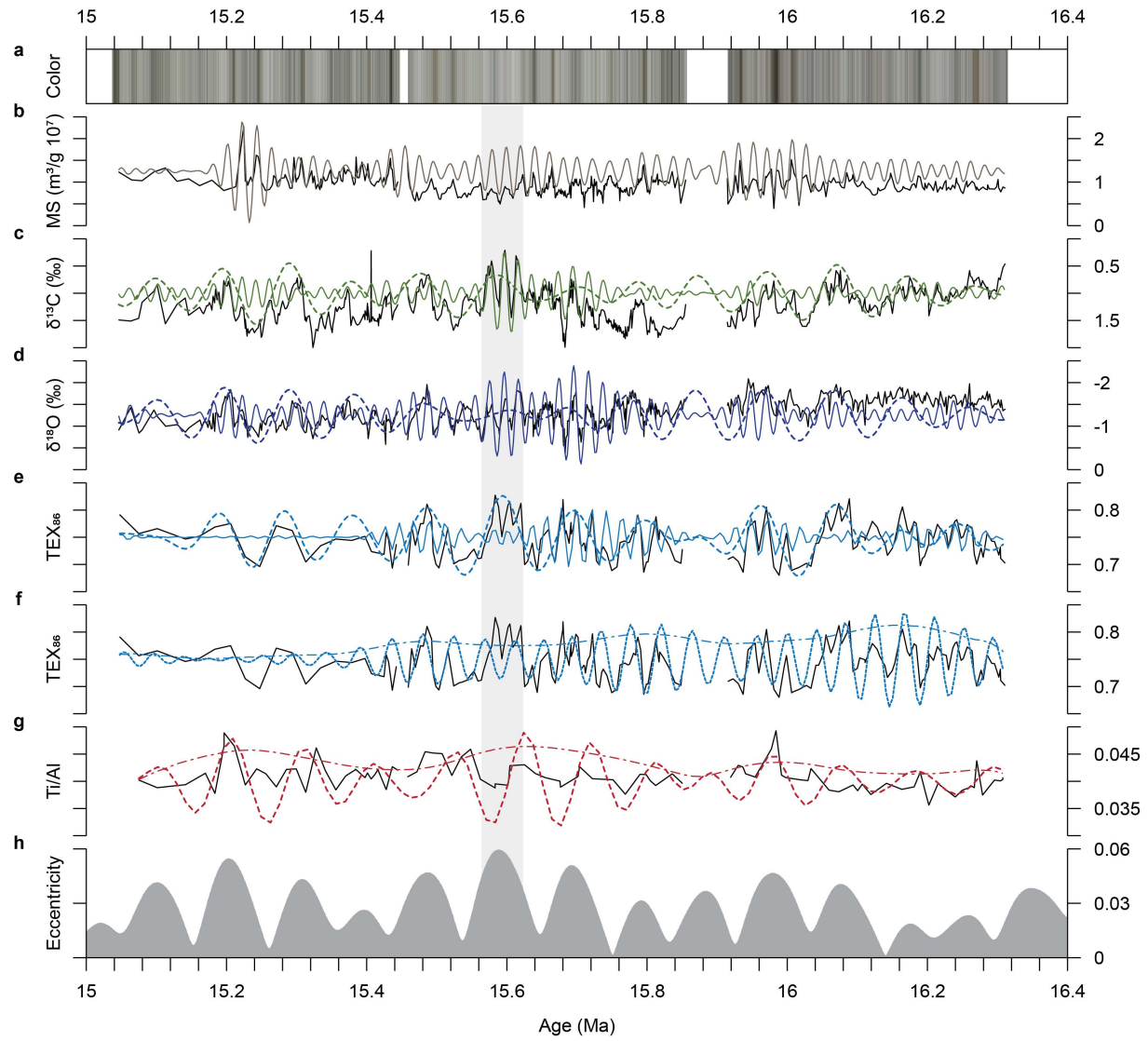

Figure 8. Interval 3 (16.3-15.0 Ma) with Site 959 proxy data and bandpass filters: (**a**) color, (**b**) MS, (**c**) $\delta^{13}C$, (**d**) $\delta^{18}O$, (**e-f**) TEX_{86}, (**g**) Ti/Al, and (**h**) the La2004 eccentricity solution (Laskar et al., 2004). The gray bar indicates the MCO 'peak warming' event at 15.6 Ma. Bandpass filters of ~100 kyr, ~60-40 kyr, and ~27-17 kyr cyclicity are represented by dashed, dotted, and solid colored lines, respectively. Amplitude modulations are represented by the dashed-dotted colored lines. The following bandpass filter widths (in 1/kyr) were used: 0.0405-0.058 for MS, 0.007-0.0135 and 0.039-0.059 for $\delta^{13}C$, 0.0085-0.0125 and 0.0405-0.0555 for $\delta^{18}O$, 0.006-0.013, 0.021-0.026 and 0.04-0.055 for TEX_{86}, and 0.008-0.0122 for Ti/Al.

5 Discussion

The Early to Middle Miocene proxy records of Site 959 reveal periodicities of ~400 and ~100 kyr, ~41 kyr, and ~27-17 kyr, which are likely related to ~400 and ~100 kyr eccentricity, obliquity, and precession, respectively, and additionally ~60-50 kyr cyclicity. Fluctuations of TEX_{86} reflect temperature variations of the shallow subsurface and were interpreted to represent

variations in upwelling intensity, consistent with dinoflagellate cyst analyses (Wubben et al., submitted). As upwelling boosts productivity, this is in agreement with the occurrence of productivity (Ba_{bio}) peaks during temperature (TEX_{86}) minima. Concurring V/Al peaks suggest reduced oxygen conditions, possibly due to increased decomposition of organic matter. Peaks of Ti/Al are interpreted as periods of increased dust supply and occurred when upwelling was intensified. Terrestrial input was mainly aeolian, as Site 959 was not strongly affected by fluvial processes during the Early to Middle Miocene (Wubben et al., submitted). These orbitally-paced variations in upwelling intensity and dust supply point to changes in atmospheric and hydrologic circulation related to the presence of a monsoon system. Here, we discuss how Site 959 was affected by monsoon dynamics and evaluate potential high-latitude influence by looking at variability and phase relations at scales of precession, obliquity, and eccentricity.

5.1 Origin of 60-50 kyr cyclicity

Significant ~60-50 kyr cyclicity is found just after the onset of the MCO (16.9-16.3 Ma) in records of wt% $CaCO_3$, TEX_{86}, Ba_{bio}, Ti/Al, and V/Al. Similarly, strong ~54 kyr cyclicity is found in the subtropical Atlantic dust record between 1 and 2 Ma (Tiedemann et al., 1994). Interestingly, the benthic $\delta^{18}O$ record remains dominated by 41 kyr obliquity in this interval (Tiedemann et al., 1994). Intermittent ~50 cyclicity has also been found in the Late Oligocene to Early Miocene $\delta^{18}O$ record from the Pacific (Beddow et al., 2018). It was suggested to be related to an offset obliquity cycle or a harmonic of the ~100 kyr eccentricity cycle (Beddow et al., 2018).

A ~54 kyr component is present in the orbital solution of obliquity (e.g., Hinnov, 2013), but it is small compared to the 41 kyr component and therefore cannot produce significant ~54 kyr variability in the proxy records. No clear correlation is found between ~100 kyr and ~60-50 kyr cyclicity (Figures 7 & 9), indicating that the latter was not a harmonic of ~100 kyr eccentricity. It seems that ~60-50 kyr cyclicity originates from ~27-17 kyr variability that is amplified every second or third cycle, similar to interference patterns between precession and obliquity in the orbital solution. Indeed, the amplitude modulation of the standardized tilt and precession (TP) curve corresponds very well with ~60-50 kyr cyclicity in the proxy records (Figure 9). This amplitude modulation cycle is dominated by power around ~60-50 kyr (Figure S4), which consists of combination tones of ~22-24 kyr precession and obliquity (frequency precession minus frequency obliquity; von Dobeneck & Schmieder, 1999). Additional power is present around ~35 kyr due to combination tone of ~19 kyr precession and obliquity, which might explain the observed ~35 cyclicity in the $\delta^{18}O$ and MS records during the MCO (Figure 5; Wubben et al., 2023). Power at ~35 kyr is weaker during ~2.4 Myr eccentricity minima (e.g., just after the MCO onset), because the ~19 kyr precession component is weaker. Therefore, we suggest that the observed ~60-50 kyr cyclicity is most likely related to combination tones of precession and obliquity.

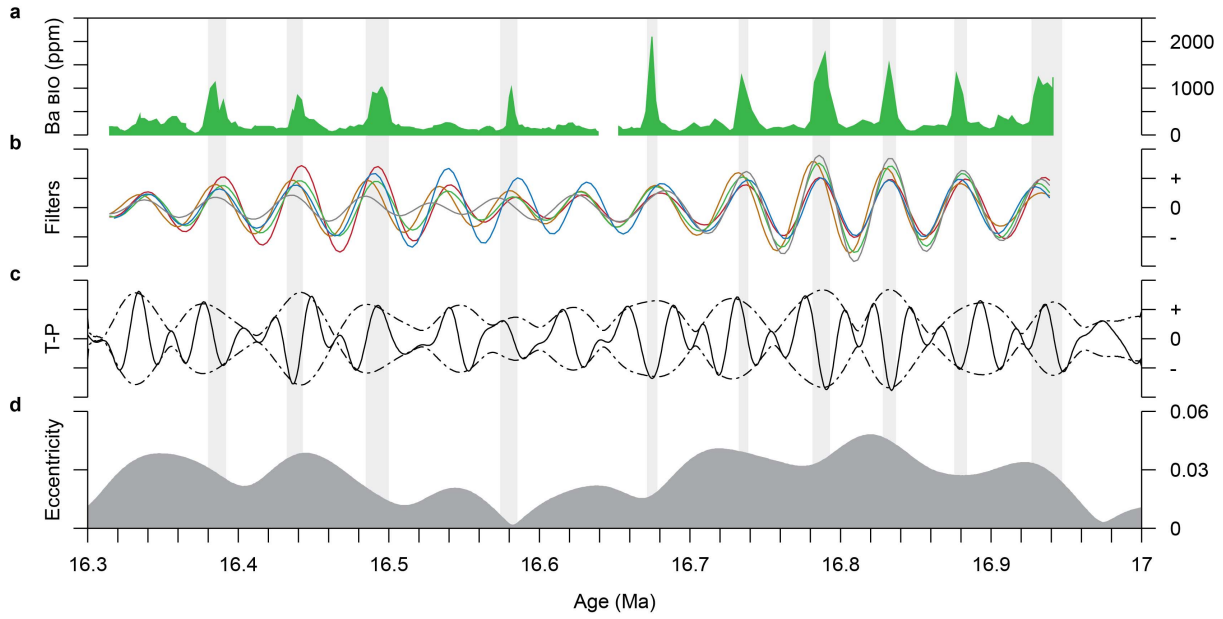

Figure 9. 60-50 kyr cyclicity in Site 959 proxy records just after the MCO onset (16.9-16.3 Ma). The Ba_{bio} record (**a**) is compared to ~60-50 kyr bandpass filters of $CaCO_3$ (gray), TEX_{86} (blue), Ba_{bio} (green), Ti/Al (red), and V/Al (orange; **b**), the standardized tilt and reversed-precession (T-P) curve (solid black) with its amplitude modulation (dashed-dotted black; **c**), and eccentricity (**d**) of the La2004 solution (Laskar et al., 2004). The gray bars indicate relatively dark sediment layers that correspond to peaks of Ba_{bio}. See caption of Figure 7 for bandpass filter widths.

5.2 Dust supply

5.2.1 Precession and obliquity phasing

At present, a large dust source is located in North Africa (Prospero et al., 2002) and NE trade winds transport dust from central North Africa to the eastern equatorial Atlantic during winter (Figure 2b; Prospero et al., 2002; Stuut et al., 2005). Aridification of North Africa occurred from the Early Miocene, during which the climate was mainly semiarid with restricted arid areas (Hounslow et al., 2017; Z. Zhang et al., 2014). Modelling studies, using relatively recent (<1 Ma) boundary conditions, show that decreased boreal summer insolation during precession maxima and obliquity minima resulted in decreased moisture transport from the tropical Atlantic towards North Africa and decreased continental precipitation in that region (Bosmans, Drijfhout, et al., 2015). This decreases vegetation cover and increases aridity, which together with wind strength/direction determines dust supply to the ocean (Trauth et al., 2009).

Just after the onset of the MCO (16.9-16.3 Ma), the Ti/Al record is strongly influenced by precession and obliquity, expressed as their combination tones. Precession-induced variations of Ti/Al also occurred in the eastern Mediterranean over at least the last 10 Myr, during which high values were linked to periods of increased aeolian versus fluvial input during precession maxima (Konijnendijk et al., 2014; Larrasoaña et al., 2003; Lourens et al., 2001; Schenau et al., 1999). Similarly, off Northwest Africa for the past 5 Myr, dust flux maxima were linked to increased South Saharan and Sahelian aridity during precession maxima (Tiedemann et al., 1994).

Although the influence of obliquity on low-latitude insolation is small, it does affect low-latitude interhemispheric insolation gradients and therefore African monsoon dynamics (Bosmans, Drijfhout, et al., 2015; Bosmans, Hilgen, et al., 2015). Obliquity signals have been recorded in dust records from the eastern Mediterranean and off Northwest Africa covering the last 3-5 Myr, with dust maxima linked to obliquity minima (Konijnendijk et al., 2014; Larrasoaña et al., 2003; Lourens et al., 2001; Tiedemann et al., 1994).

An opposite phase relationship has been assumed for Fe intensity maxima at Site 959 between 2 and 6 Ma, which generally correspond to Ti intensity and Ti/Al maxima (Figure S5; Vallé et al., 2017). Fe intensity maxima were linked to precession minima and obliquity maxima (i.e., boreal summer insolation maxima; Vallé et al., 2017). This precession phasing might be possible if dust would have originated from southern Africa, which was the case for the Cretaceous when the African continent was displaced to the south compared to the present and Miocene (Beckmann et al., 2005). However, only small dust sources are currently located in southern Africa (Prospero et al., 2002) and the Miocene continental configuration was more similar to the present than to the Cretaceous. Moreover, their age model resulted in errors up to 50 kyr for the 2.8-3.5 Ma interval, possibly due to incorrectly assumed phase relationships, and a revised age model for this interval indicates that Fe intensity maxima were related to obliquity minima (Figure S6; van der Weijst et al., 2020). Therefore, we assume that dust (Ti/Al) maxima during the Early to Middle Miocene at Site 959 were related to precession maxima and obliquity minima.

5.2.2 Eccentricity

Eccentricity is the amplitude modulator of precession and power at its frequency bands, which is basically absent in the insolation forcing, can be produced by a non-linear response to precession forcing. A significant expression of eccentricity has been found in dust records from the eastern Mediterranean, off Northwest Africa, and in the eastern equatorial Atlantic over the last 6 Myr (Larrasoaña et al., 2003; Tiedemann et al., 1994; Vallé et al., 2017). However, no significant ~100 kyr signal is present in the Early to Middle Miocene Ti/Al record (Figure 5) and its phasing relative to eccentricity is not consistent (Figure 10). Dust maxima roughly correspond to eccentricity minima between 16.7-16.3 Ma, while they mostly correspond to eccentricity maxima between 16.3-15.0 Ma. Higher amplitudes of the ~100 kyr signal approximately occur during ~400 kyr eccentricity maxima (Figure 10).

Dust maxima corresponded to eccentricity maxima in dust records off Northwest Africa between 3 and 5 Ma (Tiedemann et al., 1994) and from Site 959 between 2 and 6 Ma (Vallé et al., 2017). The dust flux was mainly dependent on low-latitude insolation forcing prior to 3 Ma, while the response was more complex after 3 Ma due to the influence of the northern hemisphere glaciations (Tiedemann et al., 1994). For the last 0.5 Myr, dust maxima off West and East Africa occurred during major ~100 kyr-driven glacials (deMenocal, 2004). Therefore, an antiphase relationship might indicate an influence of glaciations, while an in-phase relationship suggests mainly low-latitude forcing.

A relatively weak ~100 kyr but strong ~400 kyr expression has been found in the eastern Mediterranean hematite-based dust record for the last 3 Myr, with maxima corresponding to ~400 kyr eccentricity minima (Larrasoaña et al., 2003). Trauth et al. (2009) proposed that the contrasting eccentricity phasing originated from differences in dust transportation mechanisms. However, the hematite record shows a significant increase around 2.5 Ma which is not observed

for Ti/Al at the same site (Larrasoaña et al., 2003; Lourens et al., 2001), indicating that the response might also depend on the type of dust proxy. Our MS record also differs from Ti/Al, as Ti/Al peaks can corresponds to maximum or minimum MS values, possibly due to dilution effects (Wubben et al., 2023). This shows that there can be several factors that complicate the dust response to eccentricity. In addition, the signal might not be clearly recorded between 16.9 and 16.3 Ma due to the reduced power of the ~100 kyr eccentricity cycle during a ~2.4 Myr eccentricity minimum, and might be obscured between 16.3 and 15.0 Ma due to the low resultion.

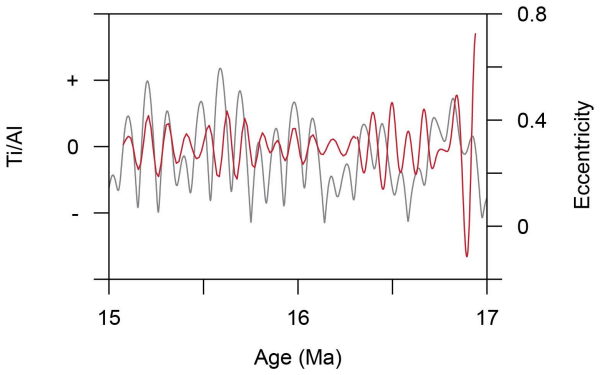

Figure 10. Bandpass filters of ~100 kyr cyclicity in the Ti/Al record (red) compared to the La2004 eccentricity solution (gray; Laskar et al., 2004) for the MCO interval (17-15 Ma). See caption of Figures 7 and 8 for bandpass filter widths.

5.3 Sea (sub)surface temperature

5.3.1 Seasonal and precession phasing of upwelling

The present-day main upwelling event in the Gulf of Guinea occurs during boreal summer. However, a more southerly position of the Guinea coast likely prevented the inflow of the NECC and EUC, the establishment of the Guinea Current, and thus the establishment of coastal upwelling during boreal summer (Figure 2c; Norris, 1998a; Wagner, 2002). In this scenario, the westward flowing SEC would be the main current in the Gulf of Guinea. Therefore, it was proposed that coastal upwelling more likely occurred during boreal winter in response to the southward displacement of the ITCZ and westward blowing surface winds, displacing surface waters to the left in the southern hemisphere (Figure 2d; Wagner, 2002). This suggests that more intense or prolonged upwelling and therefore lowest SSTs occurred during precession maxima, in response to a more/prolonged southerly position of the ITCZ (Norris, 1998a). However, considering a more southern position of Africa, it might also be possible that the Gulf of Guinea was significantly affected by the Atlantic cold tongue, which forms during early boreal summer as southeast (SE) trade winds intensify (Caniaux et al., 2011). For the last 250 kyr, it has been inferred that increased equatorial upwelling and coolest eastern equatorial SSTs occurred during precession maxima, because the SE trade winds intensify as the West African monsoon weakens (McIntyre et al., 1989). This suggests that lowest SSTs most likely occurred during precession maxima, either due to intensified coastal or equatorial upwelling.

Comparison to simulations of Atlantic SST is complicated, because they do not always incorporate differences in precession or continental configuration. As expected, a westward

flowing current dominates in the Gulf of Guinea when the Guinea coast is located just above the equator like in the Eocene simulation (Acosta et al., 2022). However, the simulations of Acosta et al. (2022) do not show significant coastal upwelling in the Gulf of Guinea in any of the Cenozoic simulations, including the preindustrial, suggesting that the model does not capture this process. In these simulations, lowest eastern equatorial SSTs occurred during boreal summer throughout the Cenozoic, which seems to be related to the Atlantic cold tongue. Bosmans, Drijfhout, et al. (2015) performed simulations with different astronomical parameters, but with a modern continental configuration, for which the SST outputs are included in our Supporting Information (Figure S7). These show lower SSTs along the Guinea coast during precession minima throughout the year, possibly related to intensified coastal upwelling under the modern land-sea distribution. Around the equator, SSTs are lower during precession minima for boreal winter and spring, but higher during precession minima for boreal autumn. The latter is in agreement with intensified equatorial upwelling during precession maxima.

5.3.2 Non-linear response

Temperature variability at Site 959 was strongly paced by ~100 kyr eccentricity prior to the MCO (17.9-17.7 Ma) and during the MCO between 16.5-15.0 Ma. The ~100 kyr signal is weak between 16.9-16.5 Ma, which is in agreement with the occurrence of a node in eccentricity (~2.4 Myr minimum) during which the amplitude of the ~100 kyr eccentricity cycle is reduced. We linked lowest temperatures to intensified upwelling during precession maxima. However, if the intensity of upwelling depended on the amplitude of precession, we would expect lowest temperatures to occur during eccentricity maxima, which is not the case. Alternatively, the degree of stratification was dependent on the amplitude of precession, resulting in greater stratification and higher temperatures during eccentricity maxima, as observed. This agrees with the increased abundance of dinoflagellate cyst *Polysphaeridium* during TEX_{86} maxima, which indicates extreme stratification of surface waters (hyperstratification; Wubben et al., submitted). The temperature sensitivity to one side of the precession cycle indicates that the response was highly non-linear (Figure 11).

The asymmetry of ~100 kyr TEX_{86} cycles prior to the MCO (17.9-17.7 Ma) and the ~60-50 kyr TEX_{86} cycle around 16.76 Ma suggests that (sub)surface temperature at Site 959 was affected by high-latitude, glacial processes (Figure 12). This agrees with occurrence of low temperatures during eccentricity minima and obliquity minima (when glacial periods are expected to occur). Asymmetric, sawtooth-shaped cycles are typical for glacial cycles of the Late Pleistocene (Lisiecki & Raymo, 2007) and are also found in the Early Miocene, linked to prolonged ice sheet growth on Antarctica and subsequent rapid retreat (Liebrand et al., 2017). The mostly symmetrical cycles during the MCO indicate a more direct response to orbital forcing, which is in line with a smaller Antarctic ice sheet that was restricted to the inner continent (Colleoni et al., 2018). However, high-latitude processes might have still contributed to the pronounced and non-linear (i.e., symmetrical but one-sided) ~100 kyr TEX_{86} signal between 16.5 and 15.0 Ma.

Antarctic terminations presumably occurred in response to austral summer insolation maxima (Holbourn et al., 2013; Holbourn et al., 2014; de Vleeschouwer et al., 2017), suggesting TEX_{86} maxima (which follow the inferred terminations) were related to precession maxima. This is in disagreement with the most likely precession phasing based on monsoon forcing. It is unlikely that the precession phasing of TEX_{86} switched throughout the Early to Middle Miocene,

because no significant changes in phasing are observed between TEX_{86} and other proxies. Throughout the 18-15 Ma interval, TEX_{86} maxima remain in phase with $\delta^{13}C$ and $\delta^{18}O$ minima, slightly lagging $\delta^{13}C$ at ~100 kyr scale and leading at precession scale (Figure S8). Potentially, the timing of the TEX_{86} maxima is determined by a combination of monsoonal and glacial forcing. During the late Pleistocene, benthic $\delta^{18}O$ lagged the summer insolation forcing by ~6 kyr for precession (e.g., Konijnendijk et al., 2015), which is half of the duration between precession maxima and minima (~11 kyr), and major deglaciations affected the timing of the African monsoon (~3 kyr lag; e.g., Grant et al., 2016). For the Miocene, it might be possible that major Antarctic deglaciations induced leads in the monsoon response, shifting TEX_{86} maxima towards the timing of ice-volume minima in between the precession extremes. A phase lead with the precession extremes can also be established if TEX_{86} responded to insolation changes earlier in the year than the solstice, resulting in a lead of ~1.8 kyr per month earlier. For example, the SE trade winds, which drive equatorial upwelling, intensify from March to mid-June (Caniaux et al., 2011). Although this might provide an explanation, the precession phasing, which is crucial for understanding the climate system, remains enigmatic.

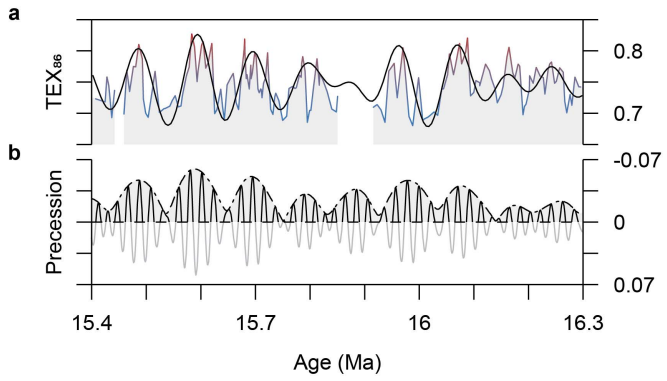

Figure 11. Non-linear TEX_{86} response between 16.3 and 15.4 Ma. The TEX_{86} record is indicated by the red-blue line (representing warmer-colder temperatures) and overlain with its bandpass filter of ~100 kyr cyclicity (black; **a**). The non-linear, one-sided response to precession (solid black/gay) is illustrated by the horizontal dached line. The amplitude of precession is modulated by eccentricity (dashed-dotted black). Precession and eccentricity are derived from the La2004 solution (Laskar et al., 2004). See caption of Figure 8 for bandpass filter width.

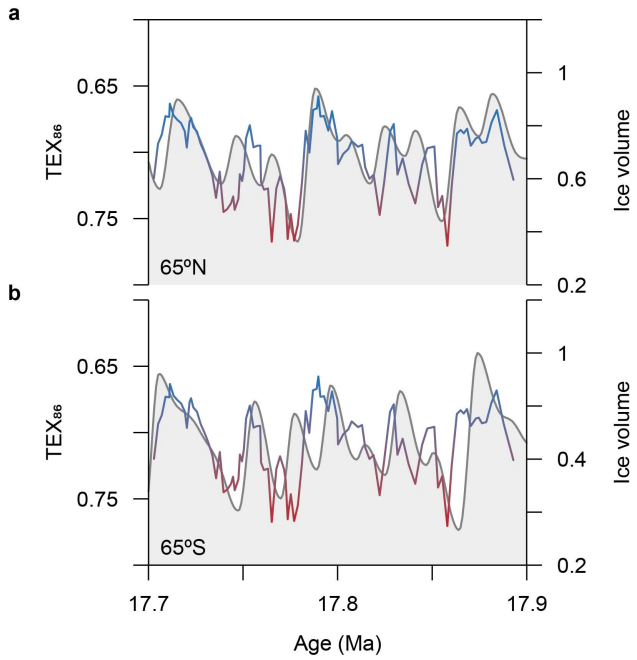

Figure 12. Asymmetric TEX_{86} cycles between 17.9 and 17.7 Ma. The TEX_{86} record is indicated by the red-blue line (representing warmer-colder temperatures) and compared to the ice volume model of Imbrie and Imbrie (1980) using insolation forcing of 65°N June 21 (**a**) and 65°S December 21 (**b**) computed with Astrochron (Meyers, 2014).

5.4 Obliquity and high-latitude influence

The influence of obliquity is recorded throughout the Early to Middle Miocene (18-15 Ma) at Site 959, expressed as ~41 kyr obliquity or as combination tones of precession and obliquity (~60-50 kyr cyclicity). A strong influence of obliquity is recorded prior to the MCO (18.2-17.7 Ma) and just after the onset of the MCO (16.9-16.3 Ma), while the effect of obliquity is expected to be much smaller than that of precession (Bosmans, Drijfhout, et al., 2015). In insolation curves, the expression of obliquity can become more evident during ~400 kyr and ~2.4 Myr eccentricity minima. This can be observed in the TEX_{86} record as an increase in amplitude modulation of ~41 kyr cyclicity during the ~400 kyr eccentricity minima around 16.2 and 15.8 Ma. Although the 16.9-16.3 Ma interval corresponds to a node in eccentricity, the very pronounced ~60-50 kyr cyclicity suggests that at least part of the obliquity influence must be derived from high-latitudes where insolation is more influenced by obliquity.

Benthic $\delta^{18}O$ records indicate that the high-latitude climate was paced by obliquity and eccentricity during the Early Miocene (Billups et al., 2004; Liebrand et al., 2016; Liebrand et al., 2017; Pälike et al., 2006) and mainly by ~100 kyr eccentricity during the Middle to Late

Miocene, with a switch to dominant obliquity pacing during eccentricity nodes around 14.4, 9.5, and 7.5 Ma (Holbourn et al., 2007; Holbourn et al., 2018). This agrees with patterns reflected in the Lower to Middle Miocene proxy records of Site 959.

High-latitude, glacial-interglacial variability (on both eccentricity and obliquity scales) might be transferred to the tropics through changes in oceanic circulation, atmospheric circulation and/or greenhouse gases. Late Pliocene TEX_{86} at Site 959, although representing a deeper signal, was also sensitive to glacial-interglacial variability and minima concurred with glacial stages (van der Weijst et al., 2022). Sub-thermocline waters at Site 959 are delivered by South Atlantic Central Water (SACW), which mixes at depth with Antarctic Intermediate Water (AAIW; van der Weijst et al., 2022). Similar to simulations for the Eocene-Oligocene transition, meridional overturning circulation and northward transport of AAIW might have been enhanced in response to Antarctic ice sheet growth (Goldner et al., 2014). This might have decreased the temperature of upwelled water at Site 959.

Additionally, colder periods on Antarctica might have intensified trade winds. For the bipolar-glaciated Pleistocene, both simulation and proxy data indicate intensification of NE trade winds during colder periods in the northern hemisphere (McGee et al., 2018). This was also suggested for the tight coupling between SST and productivity at the obliquity frequency in equatorial upwelling regions during the early Pleistocene (Cleaveland & Herbert, 2007). Oppositely, an intensification of SE trade winds has been recorded in the southeastern Atlantic during Antarctic cold periods over the last 135 kyr (Shi et al., 2001) and during Antarctic ice volume increases during the Middle to Late Miocene (Heinrich et al., 2011). As SE trade winds drive the Atlantic cold tongue (Caniaux et al., 2011), their intensification might result in lower temperatures in the eastern equatorial Atlantic.

Lastly, glacial-interglacial variations in greenhouse gases could have affected the tropical climate. Simulations show that elevated atmospheric CO_2 concentrations result in higher surface temperatures, enhancing the Atlantic ITCZ and African monsoon precipitation (Acosta et al., 2022). Therefore, lowered atmospheric CO_2 concentrations during glacial periods could have resulted in increased North African aridity and dust supply to Site 959. The strong and nearly synchronous response of tropical SSTs to obliquity during the Early Pleistocene was also attributed to glacial-interglacial greenhouse gas forcing (Cleaveland & Herbert, 2007). This indicates that the high-latitude influence on the tropics was strong even though the northern hemisphere ice sheets were still relatively small, which could be similar for the Early to Middle Miocene.

6 Conclusions

Early to Middle Miocene proxy records from Site 959 provided insights into orbitally-forced tropical climate dynamics across the prelude, onset, and continuation of the MCO (18-15 Ma). Maxima of $\delta^{13}C$ generally correspond to maxima of $\delta^{18}O$, Ba_{bio}, Ti/Al, and V/Al, minima of wt% $CaCO_3$ and TEX_{86}, and darker sediment layers which are likely rich in biogenic silica. The records revealed periodicities of ~400 and ~100 kyr, ~41 kyr, and ~27-17 kyr which are likely related to ~400 and ~100 kyr eccentricity, obliquity, and precession, respectively, and ~60-50 kyr cyclicity related to combination tones of precession and obliquity. Variability differed between proxy records and changed through time in three distinct phases: (1) strong eccentricity, obliquity and precession variability prior to the MCO (18.2-17.7 Ma), (2) strong influence of obliquity just after the onset of the MCO (16.9-16.3 Ma) oncurring within a node in the 2.4 Myr

eccentricity cycle, and (3) dominant eccentricity and precession variability between 16.3 and 15.0 Ma. Monsoon dynamics induced changes in upwelling intensity and North African aridity, resulting in low sea (sub)surface temperatures (TEX_{86}) coinciding with high productivity (Ba_{bio}) and dust input (Ti/Al) at Site 959. Because of the asymmetry of ~100 kyr TEX_{86} cycles prior to the MCO and the ~60-50 kyr TEX_{86} cycle around 16.76 Ma, strong influence of obliquity between 16.9-16.3 Ma, and non-linearity of ~100 kyr TEX_{86} variability between 16.3-15.0 Ma, it is considered likely that Site 959 was also affected by high-latitude, glacial-interglacial variability throughout the Early to Middle Miocene. Therefore, Site 959 proxy records reflect a complex system that was sensitive to seasonality, low-latitude insolation forcing, and high-latitude dynamics.

Acknowledgments

This work was funded by the European Research Council (Consolidator Grant 771497, awarded to Appy Sluijs) under the Horizon 2020 program. We thank Coen Mulder (Utrecht University) for technical support. We thank Joyce Bosmans for sharing her unpublished model results.

Conflict of Interest

The authors declare that they have no conflict of interest.

Open Research

The sediment color, MS, wt% $CaCO_3$, and bulk carbonate $\delta^{13}C$ and $\delta^{18}O$ data of Wubben et al. (2023) are available at Zenodo via https://doi.org/10.5281/zenodo.7584238.

All other data will be made available at Zenodo upon publication.

References

Acosta, R. P., Ladant, J.-B., Zhu, J., & Poulsen, C. J. (2022). Evolution of the Atlantic Intertropical Convergence Zone, and the South American and African monsoons over the past

95-Myr and their impact on the tropical rainforests. *Paleoceanography and Paleoclimatology*, *37*(7), e2021PA004383. https://doi.org/10.1029/2021PA004383

Basile, C., Mascle, J., Popoff, M., Bouillin, J. P., & Mascle , G. (1993). The Ivory Coast-Ghana transform margin: A marginal ridge structure deduced from seismic data. *Tectonophysics*, *222*(1), 1-19. https://doi.org/10.1016/0040-1951(93)90186-N

Beckmann, B., Flögel, S., Hofmann, P., Schulz, M., & Wagner, T. (2005). Orbital forcing of Cretaceous river discharge in tropical Africa and ocean response. *Nature*, *437*, 241-244. https://doi.org/10.1038/nature03976

Beddow, H. M., Liebrand, D., Wilson, D. S., Hilgen, F. J., Sluijs, A., Wade, B. S., & Lourens, L. J. (2018). Astronomical tunings of the Oligocene-Miocene transition from Pacific Ocean Site U1334 and implications for the carbon cycle. *Climate of the Past*, *14*(3), 255-270. https://doi.org/10.5194/cp-14-255-2018

Billups, K., Pälike, H., Channell, J. E. T., Zachos, J. C., & Shackleton, N. J. (2004). Astronomic calibration of the Late Oligocene through Early Miocene geomagnetic polarity time scale. *Earth and Planetary Science Letters*, *224*(1-2), 33-44. https://doi.org/10.1016/j.epsl.2004.05.004

Bloemendal, J., & deMenocal, P. (1989). Evidence for a change in the periodicity of tropical climate cycles at 2.4 Myr from whole-core magnetic susceptibility measurements. *Nature, 342*, 897-900. https://doi.org/10.1038/342897a0

Bosmans, J. H. C., Drijfhout, S. S., Tuenter, E., Hilgen, F. J., & Lourens, L. J. (2015). Response of the North African summer monsoon to precession and obliquity forcings in the EC-Earth GCM. *Climate Dynamics, 44*, 279-297. https://doi.org/10.1007/s00382-014-2260-z

694 Bosmans, J. H. C., Hilgen, F. J., Tuenter, E., & Lourens, L. J. (2015). Obliquity forcing of low-
695 latitude climate. *Climate of the Past, 11*(10), 1335-1346. https://doi.org/10.5194/cp-11-1335-
696 2015
697 Burls, N. J., Bradshaw, C. D., de Boer, A. M., Herold, N., Huber, M., Pound, M., Donnadieu, Y.,
698 Farnsworth, A., Frigola, A., Gasson, E., von der Heydt, A. S., Hutchinson, D. K., Knorr, G.,
699 Lawrence, K. T., Lear, C. H., Li, X., Lohmann, G., Lunt, D. J., Marzocchi, A., Prange, M.,
700 Riihimaki, C. A., Sarr, A.-C., Siler, N., & Zhang, Z. (2021). Simulating Miocene warmth:
701 Insights from an opportunistic multi-model ensemble (MioMIP1). *Paleoceanography and*
702 *Paleoclimatology, 36*(5), 1-40. https://doi.org/10.1029/2020PA004054
703 Calvert, S. E., & Pedersen, T. F. (2007). Chapter fourteen elemental proxies for palaeoclimatic
704 and palaeoceanographic variability in marine sediments: Interpretation and application.
705 *Developments in Marine Geology, 1*, 567-644. https://doi.org/10.1016/S1572-5480(07)01019-6
706 Caniaux, G., Giordani, H., Redelsperger, J.-L., Guichard, F., Key, E., & Wade, M. (2011).
707 Coupling between the Atlantic cold tongue and the West African monsoon in boreal spring and
708 summer. *Journal of Geophysical Research, 116*, C04003. https://doi.org/10.1029/2010JC006570
709 Cleaveland, L. C., & Herbert, T. D. (2007). Coherent obliquity band and heterogenous
710 precession band responses in early Pleistocene tropical sea surface temperatures.
711 *Paleoceanography, 22*(2), PA2216. https://doi.org/10.1029/2006PA001370
712 Colleoni, F., de Santis, L., Montoli, E., Olivo, E., Sorlien, C. C., Bart, P. J., Gasson, E. G. W.,
713 Bergamasco, A., Sauli, C., Wardell, N., & Prato, S. (2018). Past continental shelf evolution
714 increased Antarctic ice sheet sensitivity to climatic conditions. *Scientific Reports, 8*, 11323.
715 https://doi.org/10.1038/s41598-018-29718-7

716 Cramwinckel, M. J., Huber, M., Kocken, I. J., Agnini, C., Bijl, P. K., Bohaty, S. M., Frieling, J.,
717 Goldner, A., Hilgen, F. J., Kip, E. L., Peterse, F., van der Ploeg, R., Röhl, U., Schouten, S., &
718 Sluijs, A. (2018). Synchronous tropical and polar temperature evolution in the Eocene. *Nature,*
719 *559*, 382-386. https://doi.org/10.1038/s41586-018-0272-2
720 DeMenocal, P. B., Ruddiman, W. F., & Pokras, E. M. (1993). Influences of high- and low-
721 latitude processes on African terrestrial climate: Pleistocene eolian records from equatorial
722 Atlantic Ocean Drilling Program Site 663. *Paleoceanography, 8*(2), 209-242.
723 https://doi.org/10.1029/93PA02688
724 DeMenocal, P. B. (2004). African climate change and faunal evolution during the Pliocene-
725 Pleistocene. *Earth and Planetary Science Letters, 220*(1-2), 3-24. https://doi.org/10.1016/S0012-
726 821X(04)00003-2
727 De Vleeschouwer, D., Vahlenkamp, M., Crucifix, M., & Pälike, H. (2017). Alternating southern
728 and northern hemisphere climate response to astronomical forcing during the past 35 m.y.
729 *Geology, 45*(4), 375-378. https://doi.org/10.1130/G38663.1
730 Djakouré, S., Penven, P., Bourlès, B., Koné, V., & Veitch, J. (2017). Respective roles of the
731 Guinea Current and local winds on the coastal upwelling in the northern Gulf of Guinea. *Journal*
732 *of Physical Oceanography, 47*(6), 1367-1387. https://doi.org/10.1175/JPO-D-16-0126.1
733 Droz, L., Blarez, E., Mascle, J., & Boko, S. (1985). The Trou Sans Fond deep-sea fan (off Ivory
734 Coast, equatorial Atlantic). *Marine Geology, 67*(1-2), 1-11. https://doi.org/10.1016/0025-
735 3227(85)90145-8
736 Dymond, J., Suess, E., & Lyle, M. (1992). Barium in deep-sea sediment: A geochemical proxy
737 for paleoproductivity. *Paleoceanography, 7*(2), 163-181. https://doi.org/10.1029/92PA00181

738 Foster, G. L., Lear, C. H., & Rae, J. W. B. (2012). The evolution of pCO_2, ice volume and
739 climate during the Middle Miocene. *Earth and Planetary Science Letters, 341-344*, 243-254.
740 https://doi.org/10.1016/j.epsl.2012.06.007
741 Frieling, J., Peterse, F., Lunt, D. J., Bohaty, S. M., Sinninghe Damsté, J. S., Reichart, G.-J., &
742 Sluijs, A. (2019). Widespread warming before and elevated barium burial during the Paleocene-
743 Eocene Thermal Maximum: Evidence for methane hydrate release? *Paleoceanography and*
744 *Paleoclimatology, 34*(4), 546-566. https://doi.org/10.1029/2018PA003425
745 GEBCO Bathymetric Compilation Group (2022). The GEBCO_2022 Grid – A continuous
746 terrain model of the global ocean and land. *British Oceanographic Data Centre*.
747 https://doi.org/10.5285/e0f0bb80-ab44-2739-e053-6c86abc0289c
748 Goldner, A., Herold, N., & Huber, M. (2014). Antarctic glaciation caused ocean circulation
749 changes at the Eocene-Oligocene transition. *Nature, 511*, 574-577.
750 https://doi.org/10.1038/nature13597
751 Govin, A., Holzwarth, U., Heslop, D., Ford Keeling, L., Zabel, M., Mulitza, S., Collins, J. A., &
752 Chiessi, C. M. (2012). Distribution of major elements in Atlantic surface sediments (36°N-49°S):
753 Imprint of terrigenous input and continental weathering. *Geochemistry, Geophysics, Geosystems,*
754 *13*(1), 1-23. https://doi.org/10.1029/2011GC003785
755 Grant, K. M., Grimm, R., Mikolajewicz, U., Marino, G., Ziegler, M., & Rohling, E. J. (2016).
756 The timing of Mediterranean sapropel deposition relative to insolation, sea-level and African
757 monsoon changes. *Quaternary Science Reviews, 140*, 125-141.
758 https://doi.org/10.1016/j.quascirev.2016.03.026
759 Heinrich, S., Zonneveld, K. A. F., Bickert, T., & Willems, H. (2011). The Benguela upwelling
760 related to the Miocene cooling events and the development of the Antarctic Circumpolar

761 Current: Evidence from calcareous dinoflagellate cysts. *Paleoceanography, 26*(3), PA3209.
762 https://doi.org/10.1029/2010PA002065
763 Hinnov, L. A. (2013). Cyclostratigraphy and its revolutionizing applications in the earth and
764 planetary sciences. *Geological Society of America Bulletin, 125*(11-12), 1703-1734.
765 https://doi.org/10.1130/B30934.1
766 Holbourn, A., Kuhnt, W., Schulz, M., Flores, J. A., & Andersen, N. (2007). Orbitally-paced
767 climate evolution during the middle Miocene Monterey carbon-isotope excursion. *Earth and*
768 *Planetary Science Letters, 261*(3-4), 534-550. https://doi.org/10.1016/j.epsl.2007.07.026
769 Holbourn, A., Kuhnt, W., Lyle, M., Schneider, L., Romero, O., & Andersen, N. (2014). Middle
770 Miocene climate cooling linked to intensification of eastern equatorial Pacific upwelling.
771 *Geology, 42*(1), 19-22. https://doi.org/10.1130/G34890.1
772 Holbourn, A., Kuhnt, W., Clemens, S., Prell, W., & Andersen, N. (2013). Middle to Late
773 Miocene stepwise climate cooling: Evidence from a high-resolution deep water isotope curve
774 spanning 8 million years. *Paleoceanography, 28*(4), 688-699.
775 https://doi.org/10.1002/2013PA002538
776 Holbourn, A. E., Kuhnt, W., Clemens, S. C., Kochhann, K. G. D., Jöhnck, J., Lübbers, J., &
777 Andersen, N. (2018). Late Miocene climate cooling and intensification of southeast Asian winter
778 monsoon. *Nature Communications, 9*, 1584. https://doi.org/10.1038/s41467-018-03950-1
779 Holbourn, A., Kuhnt, W., Kochhann, K. G. D., Andersen, N., & Meier, K. J. S. (2015). Global
780 perturbation of the carbon cycle at the onset of the Miocene Climatic Optimum. *Geology, 43*(2),
781 123-126. https://doi.org/10.1130/G36317.1
782 Hopmans, E. C., Weijers, J. W. H., Schefuß, E., Herfort, L., Sinninghe Damsté, J. S., &
783 Schouten, S. (2004). A novel proxy for terrestrial organic matter in sediments based on branched

784 and isoprenoid tetraether lipids. *Earth and Planetary Science Letters, 224*(1-2), 107-116.
785 https://doi.org/10.1016/j.epsl.2004.05.012
786 Hounslow, M. W., White, H. E., Drake, N. A., Salem, M. J., El-Hawat, A., McLaren, S. J.,
787 Karloukovski, V., Noble, S. R., & Hlal, O. (2017). Miocene humid intervals and establishment of
788 drainage networks by 23 Ma in the central Sahara, southern Libya. *Gondwana Research, 45*,
789 118-137. https://doi.org/10.1016/j.gr.2016.11.008
790 Imbrie, J., & Imbrie, J. Z. (1980). Modeling the climatic response to orbital variations. *Science,*
791 *207*(4434), 943-953. https://doi.org/10.1126/science.207.4434.943
792 Kasten, S., Haese, R. R., Zabel, M., Ruhlemann, C., & Schulz, H. D. (2001). Barium peaks at
793 glacial terminations in sediments of the equatorial Atlantic Ocean – relicts of deglacial
794 productivity pulses? *Chemical Geology, 175*(3-4), 635-651. https://doi.org/10.1016/S0009-
795 2541(00)00377-6
796 Konijnendijk, T. Y. M., Ziegler, M., & Lourens, L. J. (2014). Chronological constraints on
797 Pleistocene sapropel depositions from high-resolution geochemical records of ODP Sites 967
798 and 968. *Newsletters on Stratigraphy, 47*(3), 263-282. https://doi.org/10.1127/0078-
799 0421/2014/0047
800 Konijnendijk, T. Y. M., Ziegler, M., & Lourens, L. J. (2015). On the timing and forcing
801 mechanisms of late Pleistocene glacial terminations: Insights from a new high-resolution benthic
802 stable oxygen isotope record of the eastern Mediterranean. *Quaternary Science Reviews, 129*,
803 308-320. https://doi.org/10.1016/j.quascirev.2015.10.005
804 Larrasoaña, J. C., Roberts, A. P., Rohling, E. J., Winklhofer, M., & Wehausen, R. (2003). Three
805 million years of monsoon variability over the northern Sahara. *Climate Dynamics, 21*, 689-698.
806 https://doi.org/10.1007/s00382-003-0355-z

807 Laskar, J., Robutel, P., Joutel, F., Gastineau, M., Correira, A. C. M., & Levrard, B. (2004). A
808 long-term numerical solution for the insolation quantities of the Earth. *Astronomy &*
809 *Astrophysics, 428*(1), 261-285. https://doi.org/10.1051/0004-6361:20041335
810 Li, M., Hinnov, L., & Kump, L. (2019). Acycle: Time-series analysis software for paleoclimate
811 research and education. *Computers and Geosciences, 127*, 12-22.
812 https://doi.org/10.1016/j.cageo.2019.02.011
813 Liebrand, D., Beddow, H. M., Lourens, L. J., Pälike, H., Raffi, I., Bohaty, S. M., Hilgen, F. J.,
814 Saes, M. J. M., Wilson, P. A., van Dijk, A. E., Hodell, D. A., Kroon, D., Huck, C. E., &
815 Batenburg, S. J. (2016). Cyclostratigraphy and eccentricity tuning of the Early Oligocene
816 through Early Miocene (30.1-17.1 Ma): Cibicides mundulus stable oxygen and carbon isotope
817 records from Walvis Ridge Site 1264. *Earth and Planetary Science Letters, 450*, 392-405.
818 https://doi.org/10.1016/j.epsl.2016.06.007
819 Liebrand, D., de Bakker, A. T. M., Beddow, H. M., Wilson, P. A., Bohaty, S. M., Ruessink, G.,
820 Pälike, H., Batenburg, S. J., Hilgen, F. J., Hodell, D. A., Huck, C. E., Kroon, D., Raffi, I., Saes,
821 M. J. M., van Dijk, A. E., & Lourens, L. J. (2017). Evolution of the early Antarctic ice ages.
822 *Proceedings of the National Academy of Sciences of the United States of America, 114*(15),
823 3867-3872. https://doi.org/10.1073/pnas.1615440114
824 Lisiecki, L. E., & Raymo, M. E. (2007). Plio-Pleistocene climate evolution: Trends and
825 transitions in glacial cycle dynamics. *Quaternary Science Reviews, 26*(1-2), 56-69.
826 https://doi.org/10.1016/j.quascirev.2006.09.005
827 Lourens, L. J., Wehausen, R., & Brumsack, H. J. (2001). Geological constraints on tidal
828 dissipation and dynamical ellipticity of the Earth over the past three million years. *Nature, 409*,
829 1029-1033. https://doi.org/10.1038/35059062

Martinez-Ruiz, F., Kastner, M., Gallego-Torres, D., Rodrigo-Gámiz, M., Nieto-Moreno, V., & Ortega-Huertas, M. (2015). Paleoclimate and paleoceanography over the past 20,000 yr in the Mediterranean Sea basins as indicated by sediment elemental proxies. *Quaternary Science Reviews, 107*(1), 25-46. https://doi.org/10.1016/j.quascirev.2014.09.018

Mascle, J., Lohmann, G. P., Clift, P. D., Akamaluk, T., Allerton, S., Ask, M. V. S., et al. (1996). *Proceedings of the Ocean Drilling Program, Initial Reports* (Vol. 159). College Station, TX: Ocean Drilling Program.

McGee, D., Moreno-Chamarro, E., Green, B., Marshall, J., Galbraith, E., & Bradtmiller, L. (2018). Hemispherically asymmetric trade wind changes as signatures of past ITCZ shifts. *Quaternary Science Reviews, 180*, 214-228. https://doi.org/10.1016/j.quascirev.2017.11.020

McIntyre, A., Ruddiman, W. F., Karlin, K., & Mix, A. C. (1989). Surface water response of the equatorial Atlantic Ocean to orbital forcing. *Paleoceanography and Paleoclimatology, 4*(1), 19-55. https://doi.org/10.1029/PA004i001p00019

Meyers, S. R. (2012). Seeing red in cyclic stratigraphy: Spectral noise estimation for astrochronology. *Paleoceanography, 27*(3), PA3328. https://doi.org/10.1029/2012PA002307

Meyers, S. R. (2014). Astrochron: An R package for astrochronology. https://cran.r-project.org/package=astrochron

Müller, R. D., Cannon, J., Qin, X., Watson, R. J., Gurnis, M., Williams, S., Pfaffelmoser, T., Seton, M., Russell, S. H. J., & Zahirovic, S. (2018). GPlates: Building a virtual Earth through deep time. *Geochemistry, Geophysics, Geosystems, 19*(7), 2243-2261. https://doi.org/10.1029/2018GC007584

Norris, R. D. (1998a). Miocene-Pliocene surface-water hydrography of the eastern equatorial Atlantic. In J. Mascle, G. P. Lohmann, & M. Moullade (Eds.), *Proceedings of the Ocean Drilling*

853 *Program, Scientific Results* (Vol. 159, pp. 539-555). College Station, TX: Ocean Drilling
854 Program.
855 Norris, R. D. (1998b). Planktonic foraminifer biostratigraphy: Eastern equatorial Atlantic. In J.
856 Mascle, G. P. Lohmann, & M. Moullade (Eds.), *Proceedings of the Ocean Drilling Program,*
857 *Scientific Results* (Vol. 159, pp. 445-479). College Station, TX: Ocean Drilling Program.
858 Pälike, H., Frazier, J., & Zachos, J. C. (2006). Extended orbitally forced paleoclimatic records
859 from the equatorial Atlantic Ceara Rise. *Quaternary Science Reviews, 25*(23-24), 3138-3149.
860 https://doi.org/10.1016/j.quascirev.2006.02.011
861 Piela, C., Lyle, M., Marcantonio, F., Baldauf, J., & Olivarez Lyle, A. (2012). Biogenic
862 sedimentation in the equatorial Pacific: Carbon cycling and paleoproduction, 12-24 Ma.
863 *Paleoceanography, 27*(2). https://doi.org/10.1029/2011PA002236
864 Prospero, J. M., Ginoux, P., Torres, O., Nicholson, S. E., & Gill, T. E. (2002). Environmental
865 characterization of global sources of atmospheric soil dust identified with the Nimbus 7 Total
866 Ozone Mapping Spectrometer (TOMS) absorbing aerosol product. *Reviews of Geophysics, 40*(1),
867 1002. https://doi.org/10.1029/2000RG000095
868 Reitz, A., Pfeifer, K., de Lange, G. J., & Klump, J. (2004). Biogenic barium and the detrital
869 Ba/Al ratio: A comparison of their direct and indirect determination. *Marine Geology, 204*(3-4),
870 289-300. https://doi.org/10.1016/S0025-3227(04)00004-0
871 Rossignol-Strick, M. (1983). African monsoons, an immediate climate response to orbital
872 insolation. *Nature, 304*, 46-49. https://doi.org/10.1038/304046a0
873 Schenau, S. J., Antonarakou, A., Hilgen, F. J., Lourens, L. J., Nijenhuis, I. A., van der Weijden,
874 C. H., & Zachariasse, W. J. (1999). Organic-rich layers in the Metochia section (Gavdos,

875 Greece): Evidence for a single mechanism of sapropel formation during the past 10 My. *Marine*
876 *Geology, 153*(1-4), 117-135. https://doi.org/10.1016/S0025-3227(98)00086-3
877 Schouten, S., Hopmans, E. C., Schefuß, E., & Sinninghe Damsté, J. S. (2002). Distributional
878 variations in marine crenarchaeotal membrane lipids: A new tool for reconstructing ancient sea
879 water temperatures? *Earth and Planetary Science Letters, 204*(1-2), 265-274.
880 https://doi.org/10.1016/S0012-821X(02)00979-2
881 Seton, M., Müller, R. D., Zahirovic, S., Gaina, C., Torsvik, T., Shephard, G., Talsma, A., Gurnis,
882 M., Turner, M., Maus, S., & Chandler, M. (2012). Global continental and ocean basin
883 reconstructions since 200 Ma. *Earth-Science Reviews, 113*(3-4), 212-270.
884 https://doi.org/10.1016/j.earscirev.2012.03.002
885 Shafik, S., Watkins, D. K., & Chul Shin, I. (1998). Upper Cenozoic calcareous nannofossil
886 biostratigraphy Côte d'Ivoire-Ghana Margin, eastern equatorial Atlantic. In J. Mascle, G. P.
887 Lohmann, & M. Moullade (Eds.), *Proceedings of the Ocean Drilling Program, Scientific Results*
888 (Vol. 159, pp. 509-523). College Station, TX: Ocean Drilling Program.
889 Shi, N., Schneider, R., Beug, H.-J., & Dupont, L. (2001). Southeast trade wind variations during
890 the last 135 kyr: Evidence from pollen spectra in eastern south Atlantic sediments. *Earth and*
891 *Planetary Science Letters, 187*(3-4), 311-321. https://doi.org/10.1016/S0012-821X(01)00267-9
892 Sosdian, S. M., Greenop, R., Hain, M. P., Foster, G. L., Pearson, P. N., & Lear, C. H. (2018).
893 Constraining the evolution of Neogene ocean carbonate chemistry using the boron isotope pH
894 proxy. *Earth and Planetary Science Letters, 498*, 362-376.
895 https://doi.org/10.1016/j.epsl.2018.06.017
896 Steinthorsdottir, M., Coxall, H. K., de Boer, A. M., Huber, M., Barbolini, N., Bradshaw, C. D.,
897 Burls, N. J., Feakins, S. J., Gasson, E., Henderiks, J., Holbourn, A. E., Kiel, S., Kohn, M. J.,

898 Knorr, G., Kürschner, W. M., Lear, C. H., Liebrand, D., Lunt, D. J., Mörs, T., Pearson, P. N.,
899 Pound, M. J., Stoll, H., & Strömberg, C. A. E. (2021). The Miocene: The future of the past.
900 *Paleoceanography and Paleoclimatology, 36*(4), e2020PA004037.
901 https://doi.org/10.1029/2020PA004037
902 Steinthorsdottir, M., Vajda, V., & Pole, M. (2019). Significant transient pCO_2 perturbation at the
903 New Zealand Oligocene-Miocene transition recorded by fossil plant stomata. *Palaeogeography,*
904 *Palaeoclimatology, Palaeoecology, 515*, 152-161. https://doi.org/10.1016/j.palaeo.2018.01.039
905 Stoll, H. M., Guitian, J., Hernandez-Almeida, I., Mejia, M., Phelps, S., Polissar, P., Rosenthal,
906 Y., Zhang, H., & Ziveri, P. (2019). Upregulation of phytoplankton carbon concentrating
907 mechanisms during low CO_2 glacial periods and implications for the phytoplankton pCO_2 proxy.
908 *Quaternary Science Reviews, 208*, 1-20. https://doi.org/10.1016/j.quascirev.2019.01.012
909 Stuut, J. B., Zabel, M., Ratmeyer, V., Helmke, P., Schefuß, E., Lavik, G., & Schneider, R.
910 (2005). Provenance of present-day eolian dust collected off NW Africa. *Journal of Geophysical*
911 *Research: Atmospheres, 110*, D04202. https://doi.org/10.1029/2004JD005161
912 Super, J. R., Thomas, E., Pagani, M., Huber, M., O'Brien, C., & Hull, P. M. (2018). North
913 Atlantic temperature and pCO_2 coupling in the early-middle Miocene. *Geology, 46*(6), 519-522.
914 https://doi.org/10.1130/G40228.1
915 Thomson, D. J. (1982). Spectrum estimation and harmonic analysis. *Proceedings of the IEEE,*
916 *70*(9), 1055-1096. https://doi.org/10.1109/PROC.1982.12433
917 Tiedemann, R., Sarnthein, M., & Shackleton, N. J. (1994). Astronomic timescale for the Pliocene
918 Atlantic $\delta^{18}O$ and dust flux records of Ocean Drilling Program Site 659. *Paleoceanography,*
919 *9*(4), 619-638. https://doi.org/10.1029/94PA00208

Torsvik, T. H., van der Voo, R., Preeden, U., Mac Niocaill, C., Steinberger, B., Doubrovine, P. V., van Hinsbergen, D. J. J., Domeier, M., Gaina, C., Tohver, E., Meert, J.G., McClausland, P. J. A., & Cocks, L. R. M. (2012). Phanerozoic polar wander, paleogeography and dynamics. *Earth-Science Reviews, 114*(3-4), 325-368. https://doi.org/10.1016/j.earscirev.2012.06.007

Trauth, M. H., Larrasoaña, J. C., & Mudelsee, M. (2009). Trends, rhythms and events in Plio-Pleistocene African climate. *Quaternary Science Reviews, 28*(5-6), 399-411. https://doi.org/10.1016/j.quascirev.2008.11.003

Vallé, F., Westerhold, T., & Dupont, L. M. (2017). Orbital-driven environmental changes recorded at ODP Site 959 (eastern equatorial Atlantic) from the Late Miocene to the Early Pleistocene. *International Journal of Earth Sciences, 106*, 1161-1174. https://doi.org/10.1007/s00531-016-1350-z

Van der Weijst, C. M. H., Winkelhorst, J., Lourens, L., Raymo, M. E., Sangiorgi, F., & Sluijs, A. (2020). A ternary mixing model approach using benthic foraminifer $\delta^{13}C$- $\delta^{18}O$ data to reconstruct Late Pliocene deep Atlantic water mass mixing. *Paleoceanography and Paleoclimatology, 35*(12), e2019PA003804. https://doi.org/10.1029/2019PA003804

Van der Weijst, C. M. H., van der Laan, K. J., Peterse, F., Reichart, G.-J., Sangiorgi, F., Schouten, S., Veenstra, T. J. T., & Sluijs, A. (2022). A 15-million-year surface- and subsurface-integrated TEX_{86} temperature record from the eastern equatorial Atlantic. *Climate of the Past, 18*(8), 1947-1962. https://doi.org/10.5194/cp-18-1947-2022

Vincent, E., & Berger, W. H. (1985). Carbon dioxide and polar cooling in the Miocene: The Monterey hypothesis. In E. T. Sundquist, & W. S. Broecker (Eds.), *The Carbon Cycle and Atmospheric CO2: Natural Variations Archean to Present* (Vol. 32, pp. 455-468). Washington, DC: American Geophysical Union. https://doi.org/10.1029/GM032p0455

943 Von Dobeneck, T., & Schmieder, F. (1999). Using rock magnetic proxy records for orbital
944 tuning and extended time series analyses into the super- and sub-Milankovitch bands. In G.
945 Fischer, & G. Wefer (Eds.), *Use of proxies in paleoceanography* (pp. 601-633). Berlin,
946 Heidelberg: Springer. https://doi.org/10.1007/978-3-642-58646-0_25
947 Wagner, T. (1998). Pliocene-Pleistocene deposition of carbonate and organic carbon at Site 959:
948 Paleoenvironmental implications for the eastern equatorial Atlantic off the Ivory Coast/Ghana. In
949 J. Mascle, G. P. Lohmann, & M. Moullade (Eds.), *Proceedings of the Ocean Drilling Program,*
950 *Scientific Results* (Vol. 159, pp. 557-574). College Station, TX: Ocean Drilling Program.
951 Wagner, T. (2002). Late Cretaceous to early Quaternary organic sedimentation in the eastern
952 equatorial Atlantic. *Palaeogeography, Palaeoclimatology, Palaeoecology, 179*(1-2), 113-147.
953 https://doi.org/10.1016/S0031-0182(01)00415-1
954 Wang, P. (2009). Global monsoon in a geological perspective. *Chinese Science Bulletin, 54*,
955 1113-1136. https://doi.org/10.1007/s11434-009-0169-4
956 Weber, S. L., & Teunter, E. (2011). The impact of varying ice sheets and greenhouse gases on
957 the intensity and timing of boreal summer monsoons. *Quaternary Science Reviews, 30*(3-4), 469-
958 479. https://doi.org/10.1016/j.quascirev.2010.12.009
959 Weijers, J. W. H., Schouten, S., Spaargaren, O. C., & Sinninghe Damsté, J. S. (2006).
960 Occurrence and distribution of tetraether membrane lipids in soils: Implications for the use of the
961 TEX_{86} proxy and the BIT index. *Organic Geochemistry, 37*(12), 1680-1693.
962 https://doi.org/10.1016/j.orggeochem.2006.07.018
963 Westerhold, T., Marwan, N., Drury, A. J., Liebrand, D., Agnini, C., Anagnostou, E., Barnet, J. S.
964 K., Bohaty, S. M., de Vleeschouwer, D., Florindo, F., Frederichs, T., Hodell, D. A., Holbourn, A.
965 E., Kroon, D., Lauretano, V., Littler, K., Lourens, L. J., Lyle, M., Pälike, H., Röhl, U., Tian, J.,

966 Wilkens, R. H., Wilson, P. A., & Zachos, J. C. (2020). An astronomically dated record of Earth's
967 climate and its predictability over the last 66 million years. *Science, 369*(6509), 1383-1387.
968 https://doi.org/10.1126/science.aba6853
969 Woodruff, F., & Savin, S. M. (1991). Mid-Miocene isotope stratigraphy in the deep sea: High-
970 resolution correlations, paleoclimatic cycles, and sediment preservation. *Paleoceanography and*
971 *Paleoclimatology, 6*(6), 755–806. https://doi.org/10.1029/91PA02561
972 Wubben, E., Spiering, B., Veentra, T., Bos, R., Wang, Z., van Dijk, J., Raffi, I., Witkowski, J.,
973 Hilgen, F., Peterse, F., Sangiorgi, F., & Sluijs, A. (submitted). Tropical warming and
974 intensification of the West African monsoon during the Miocene Climatic Optimum. Submitted
975 to *Paleoceanography and Paleoclimatology* as companion paper.
976 Wubben, E., Veenstra, T., Witkowski, J., Raffi, I., Hilgen, F., Bos, R., van Dijk, J., Lathouwers,
977 Y., Spiering, B., Vennema, L., Wang, Z., Sangiorgi, F., & Sluijs, A. (2023). Astrochronology of
978 the Miocene Climatic Optimum record from Ocean Drilling Program Site 959 in the eastern
979 equatorial Atlantic. *Newsletters on Stratigraphy, 56*(4), 457-484.
980 https://doi.org/10.1127/nos/2023/0749
981 Zhang, Y. G., Pagani, M., Liu, Z., Bohaty, S. M., & DeConto, R. (2013). A 40-million-year
982 history of atmospheric CO_2. *Philosophical Transactions of the Royal Society A, 371*, 20130096.
983 https://doi.org/10.1098/rsta.2013.0096
984 Zhang, Z., Ramstein, G., Schuster, M., Li, C., Contoux, C., & Yan, Q. (2014). Aridification of
985 the Sahara desert caused by Tethys Sea shrinkage during the Late Miocene. *Nature, 513*, 401-
986 404. https://doi.org/10.1038/nature13705